Phase Sensitive MRI and its Application to Cardiovascular Diseases

Haining Liu

A dissertation
submitted in partial fulfillment of the
requirements for the degree of

Doctor of Philosophy

University of Washington

2017

Reading Committee:

Chun Yuan, Chair

Ruikang Wang

Alberto Aliseda

Program Authorized to Offer Degree:
Bioengineering

University of Washington

Abstract

Phase Sensitive MRI and its Application to Cardiovascular Diseases

Haining Liu

Chair of the Supervisory Committee:
PhD Chun Yuan
Department of Bioengineering

Inversion recovery phase sensitive (IRPS) imaging is a T1 weighted magnetic resonance imaging(MRI) method and its T1 contrast is introduced by a 180^o radio frequency(RF) pulse. IRPS image keeps the polarity map and has strong T1 contrast with flexible inversion time(TI). IRPS is used in a number of clinical applications such as myocardial scar detection and atherosclerosis evaluation. To reconstruct the IRPS images, however, a fully sampled reference scan is usually needed to help remove the background phase. This extra reference scan doubles the scan time and restrict its application to 3D imaging, especially the 3D myocardial late gadolinium enhancemen(LGE) imaging. Besides, this reference scan may introduce artifacts to the reconstructed phase sensitive images.

Motivated by this issue, in the first part of this dissertation, 3D true phase polarity recovery with independent phase estimation using the three-layer stacks based region-growing (3D-TRIPS) was proposed to directly reconstruct the inversion recovery phase sensitive images without the reference scan. Supported by theoretical simulation, a structure containing three-layer stacks is designed to optimize the region-growing track based on the signal intensity. 3D-TRIPS was evaluated on 15 patients and was compared with phase sensitive inversion recovery reconstruction(PSIR). The results show good polarity consistency between two reconstructions and 3D-TRIPS images have similar or better image quality relative to PSIR images.

IRPS images provide two types of contrast: intensity contrast and polarity contrast. The binary polarity contrast of IRPS images has not been used to directly identify the tissue boundary. In the second part of this thesis, carotid lumen identified by the negative polarity map of simultaneous noncontrast angiography and intraplaque hemorrhage(SNAP) magnetic resonance angiography(MRA) was evaluated against 3D time of flight(TOF) and contrast enhanced MRA(CE-MRA). SNAP showed a good agreement with CE-MRA in measuring both lumen area and percent stenosis. And the binary polarity map of SNAP MRA is less sensitive to flow artifacts relative to the gradient map, which was used to identify the lumen boundary of TOF. This study shows the potential of IRPS imaging on automatic segmentation and quantification of tissues of interest assisted by its binary polarity map.

Since the negative polarity map of SNAP MRA is proved to be reliable to identify the lumen boundary, in the last section of the dissertation, the lumen of SNAP MRA was firstly transferred to the magnitude part of the reference image to produce the grey-blood proton density(PD) weighted images which can be used to detect the calcified nodules near the thin fibrous cap. Besides, SNAP-motion sensitized driven equilibrium(MSDE) sequence was proposed to directly produce the grey blood PD weighted images on intracranial arteries. Furthermore, to separate the arteries from veins on SNAP, improved SNAP(iSNAP) was developed, and a binary polarity mask transferred from the difference between two different SNAP scan was used to suppress the venous lumen signal.

In conclusion, phase of complex signal plays an important role in MRI, in terms of improving tissue contrast and differentiating moving and stationary tissues. But its application has been difficult because of background phase and complex structure and SNR distributions and therefore, extra scan is usually in need to help remove the background phase. This thesis works to improve the efficiency of phase sensitive reconstruction and acquisition and therefore allows more application scenarios of phase sensitive imaging.

TABLE OF CONTENTS

LIST OF FIGURES

LIST OF TABLES

ACKNOWLEDGMENTS

I am grateful to all the members of my supervisory committee, Dr. Chun Yuan(Chair), Dr. Jeng Neng Hwang (GSR), Dr. Ruikang Wang, Dr. Alberto Aliseda and Dr. Colin Studholme for their guidance and supervision throughout my whole graduate study. I would like to thank Dr. Jinnan Wang, Dr. Gregory J. Wilson, Dr. Jeffrey Maki, Dr. Zechen Zhou, Wenchuan Wu, Dr. Jie Sun, Dr. Niranjan Balu, Dr. Baocheng Chu, Dr. Gador Canton, Dr. William S. Kerwin, Haikun Qi, Shuo Chen, Tong Zhu, Daniel Hippe, Dr. Hiroko Watase, Ms. Marina Ferguson, Zach Miller, Ms. Kristi Pimentel, Dr. Dongxiang Xu, Dr. Can Wu, Jin Liu and all the current and previous members of the Vascular Imaging Lab(VIL), for their selfless help and supports whenever there is a need.

Finally, I would like to thank my parents and my wife. I won't be able to complete the extensive study and research work without their understanding and consistent supports throughout the past years.

DEDICATION

to my dear wife Wei Wu and my parents

.

Chapter 1

INTRODUCTION

1.1 Phase of MRI signal

Compared with other imaging modalities, such as CT and ultrasound, MRI has advantage in soft tissue contrast and therefore is widely used clinically. For MRI acquisitions, with ideal acquisition conditions, especially homogeneous magnetic field, there should be no phase with MRI signal. However, ideal acquisition is hard to achieve in reality and due to the sub-optimal acquisition conditions, extra phase is added to the MRI signal and transfer the real MRI signal to a complex image which has a real part and imaginary part. Based on the summarization of literature [1, 2, 3], the complex MRI signal can be expressed as:

$$\rho(\vec{n}) = \rho_m(\vec{n})(e^{-i(\theta+2\pi\Delta B_0(\vec{n})\gamma TE+2\pi\Delta\gamma B_0 TE+g(\gamma,B_0,B_1(\omega,\vec{n}),TE))} + \frac{\rho_{noise}(\vec{n})}{\rho_m(\vec{n})}e^{-i\psi_{noise}(\vec{n})}) \quad (1.1)$$

Where ρ_m represents the magnitude of the MRI signal located at $\vec{n}$. θ represents the true phase[4]. θ is usually introduced by an extra radio frequency(RF) preparation pulse. For example, π can be introduced to θ by a 180^o inversion recovery RF pulse.

γ and $\Delta\gamma$: γ represents the gyromagnetic ratio of water, which is 42.6 $MHzT^{-1}$. $\Delta\gamma$ represents the relative gyromagnetic ratio of tissues to water[3]. The fat is the most widely existed component with chemical shift of 3.5 ppm relative to water. As can be seen from the above equation, the phase introduced by chemical shift also correlates with TE.

B_0 and ΔB_0: B_0 and ΔB_0 represent the B_0 field and the suboptimal B_0 field respectively. Several factors contribute to the suboptimal B_0 field. One is related to the scanner system itself. For example, the B_0 field from body coil cannot be perfectly homogeneous within a large FOV and therefore is influenced by the relative position to the body coil. Another source of local suboptimal B_0 field is the distribution of susceptibility. The correlation

between the changed $B_0(\Delta B_{susceptability})$ field and susceptibility distribution is shown as[2]:

$$\Delta B_{susceptability}(\vec{n}) = G(\vec{n})\Delta\chi(\vec{n})B_0 \tag{1.2}$$

$\Delta\chi$ represents the relative local magnetic susceptibility and G represents the geometry factor. G factor is variant for different subjects at different locations. Generally, larger susceptibility difference and sharper structure will introduce larger local B_0 field inhomogeneity.

$g(\gamma, B_0, B_1(\omega, \vec{n}), TE))$ represents the phase introduced by the non-linear correlation of the acquisition factors.

$\frac{\rho_{noise}(\vec{n})}{\rho_m(\vec{n})}e^{-i\psi_{noise}(\vec{n})}$ represents the phase from the noise where $\rho_{noise}(\vec{n})$ and $\rho_m(\vec{n})$ are the signal intensity of noise and MRI signal respectively. Its influence is determined by $\frac{\rho_{noise}(\vec{n})}{\rho_m(\vec{n})}$ which inversely correlates with SNR.

Another important source of the phase of MRI signals is the sensitivity map of the receiver coils[5]. And its influence can be expressed as:

$$\rho_{acquired}(\vec{n}) = \sum f(\rho(\vec{n}) \times \rho_{sensitivity,i}(\vec{n})e^{-i\psi_{sensitivity,i}(\vec{n})}) \tag{1.3}$$

where $\rho_{sensitivity,i}$ and $\psi_{sensitivity,i}$ represent the phase and magnitude part of the sensitivity map of the ith receiver coil. $\sum f(*)$ represents the multi-coil combination method. Similar to the body coil B_0 field inhomogeneity, the sensitivity map is also determined by the relative position to the receiver coil.

In summary, among the phase sources, only θ is introduced through the sequence design. Other phase sources are relevant to the scan system and the scanned subjects. And these phases are regarded as background phase[4, 6]. Several background phase sources, including true phase, chemical shift and susceptibility, reflect the physical properties of the scanned subjects. These valuable information, however, is covered up by the phase caused by the sub-optimality of scan system and therefore cannot be used directly. This problem is especially challenging with low SNR and poor B_0 field homogeneity of early MRI scanners. Over the past decades, much progress has been made to extract clinical information from MRI phase especially thanks to the improvement of MRI system. Several related applications will be introduced below.

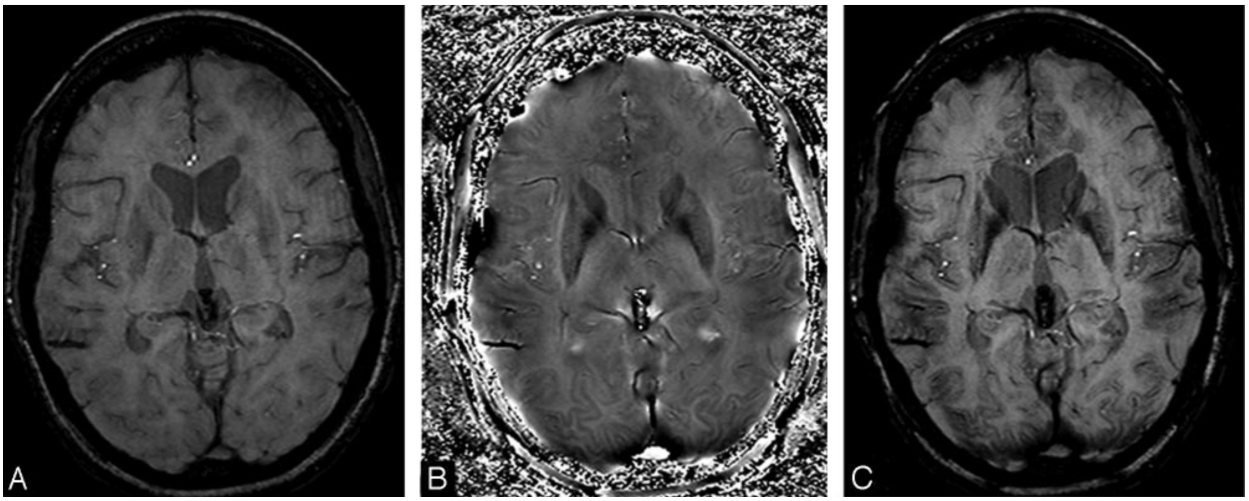

Figure 1.1: (A) is the magnitude of the unprocessed susceptibility-weighted imaging (SWI) image. (B) is the high-pass filtered phase image and (C) is the processed SWI magnitude image where veins have uniform hypo-intense signal.

1.1.1 Susceptibility-Weighted Imaging (SWI)[1, 2]

SWI is the MRI method that explores the phase introduced by the local susceptibility difference. Susceptibility is the parameter used to evaluate the change of local B_0 field caused by the tissues. Paramagnetic tissues like iron enhance the B_0 field while the diamagnetic tissues reduce the local B_0 field[2]. This phase from susceptibility $\varphi_{susceptability}$ can be expressed as: $\varphi_{susceptability} = \gamma \Delta B_{susceptability} TE$.For SWI, to extract $\varphi_{susceptability}$, a long enough TE and relatively smooth ΔB_{system}, which represents the sub-optimal B_0 field caused by the factors other than susceptibility, are required and $\varphi_{susceptability}$ can be separated from other background phase using a high-pass filter. The extracted $\varphi_{susceptability}$ can then be combined with magnitude image to identify venous blood, hemorrhage and iron storage(Figure 1.1[2]), which have big susceptibility difference relative to surrounding tissues.

1.1.2 Water-fat quantification

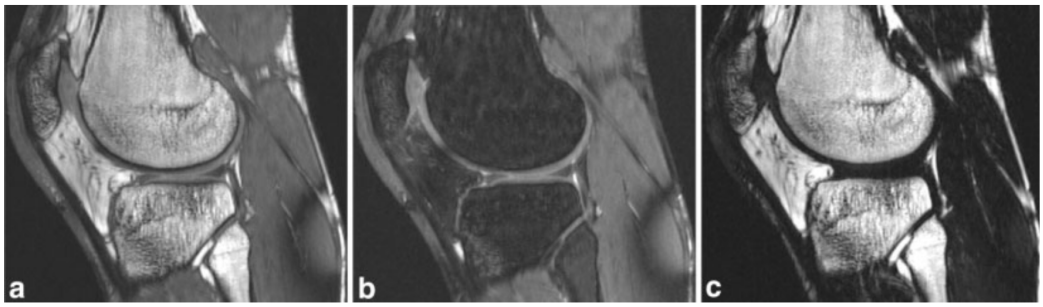

Figure 1.2: (a) is the sagittal images from the knee of a volunteer. (b) and (c) are the calculated water and fat images with Iterative decomposition of water and fat with echo asymmetry and least-squares estimation (IDEAL) method

Chemical shift of fat is another important source of background phase. A voxel with both water and fat can be expressed with a more detailed equation[7]:

$$S = A_{water}(1 + \frac{A_{fat}}{A_{water}} e^{i\Delta\gamma B_0 TE}) e^{i\gamma\Delta B_0 TE} \tag{1.4}$$

In this equation, there are three unknown parameters:$A_{fat}, A_{water}, and \Delta B_0$. Iterative decomposition of water and fat with echo asymmetry and least-squares estimation (IDEAL) method uses multiple acquisitions at different TE (≥ 3) to calculate the three parameters and therefore quantify the water/fat ratio(Figure 1.2[7]). Another water/fat quantification solution is to use a pair of optimize TEs which make $\Delta\gamma B_0 TE$ equal to 0 or π to remove the influence of chemical shift phase. To remove the polarity change caused by ($\gamma\Delta B_0 TE$), region-growing is used to estimate ($\gamma\Delta B_0 TE$). Similar with SWI, water/fat quantification is also based on the hypothesis that this phase is spatially smooth and therefore only eligible for the MRI system with good B_0 field homogeneity.

1.2 Phase sensitive inversion recovery MRI imaging

Unlike other phase based MRI methods, the phase of interest in the phase sensitive image is introduced by an inversion recovery RF pulse.

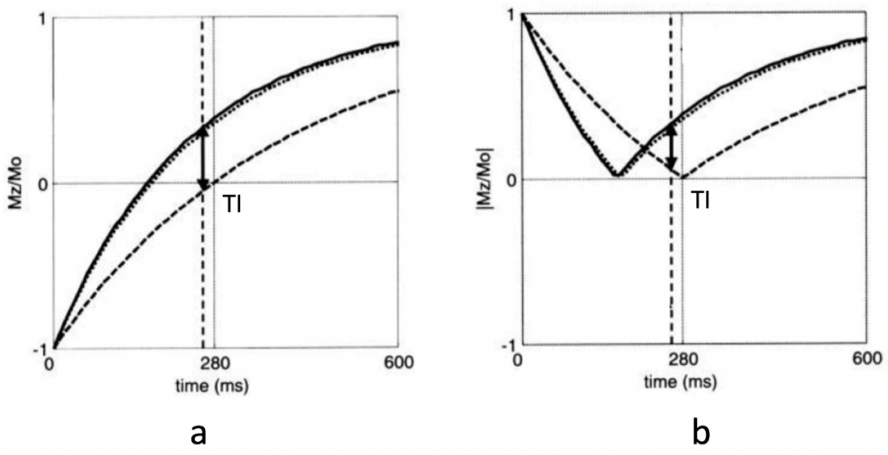

Figure 1.3: Release trajectory of two tissues with different T1 after applying a 180^o inversion pulse. At the imaging time(TI), the tissue with relative long T1 has relatively smaller signal intensity while that of shorter T1 has relatively larger signal(a). In the magnitude part(b) of the inversion recovery image, however, the contrast between two tissues is compromised.

After applying the 180^o inversion pulse (Figure 1.3a[6]), at the inversion time(TI), when the contrast between tissues of interest is optimized, θ is 0 when the signal of voxel is above 0 and π when the signal is below zero. With conventional MRI acquisition, θ is covered up by the background phase. Therefore, only the magnitude can be directly used which has reduced contrast compared with complex images (Figure 1.3b[6]) because of the inversion of negative signal. To maximize the contrast between two tissues of interest in the magnitude image, acquisition parameters, especially TI, need to be optimized so that at TI, tissue with relatively longer T1 is around zero [6]. Any TI other than the optimized TI will compromise the image contrast(Figure 1.3b[6]).

Equation 1.1 demonstrates that major sources of background phase ($2\pi\Delta B_0\gamma TE, 2\pi\Delta\gamma B_0 TE$ and $\varphi_{sensitivity,i}$) can be reproduced with the similar acquisition parameters, especially TE, of the T1 weighted image. Based on this strategy, phase sensitive inversion recovery (PSIR) was developed. With PSIR, a fully sampled reference scan was acquired after the inversion

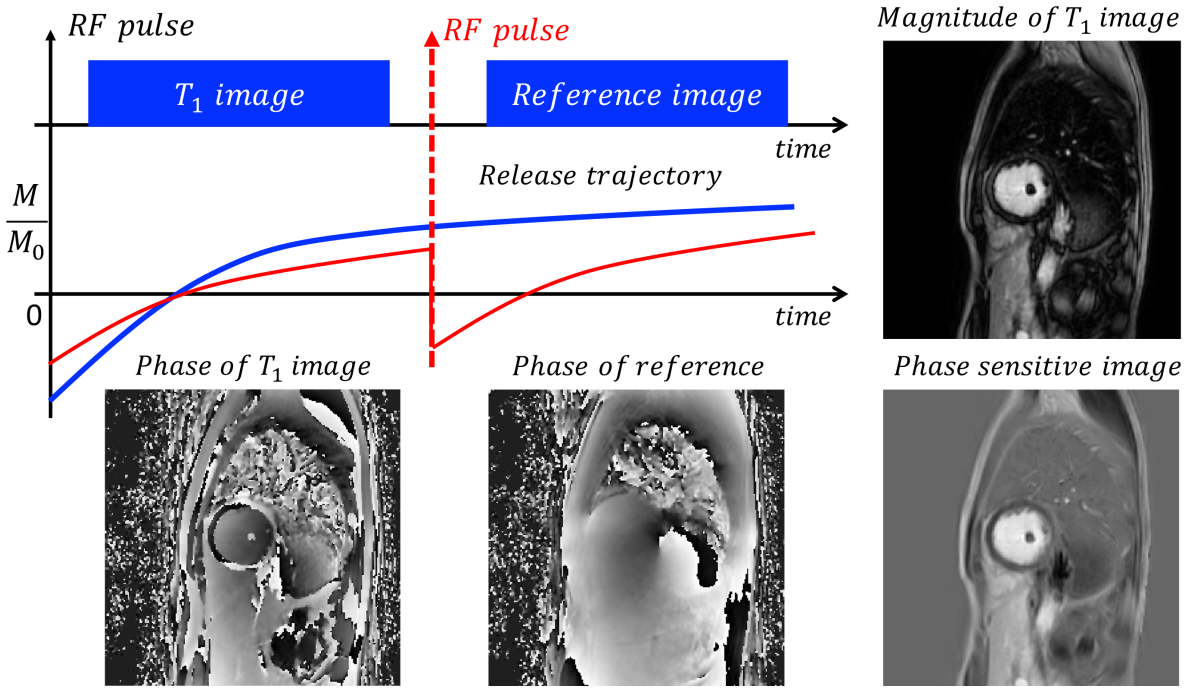

Figure 1.4: Phase sensitive reconstruction with a reference scan. A fully sampled reference scan was acquired to help remove the background phase of the T1 weighted image. Besides, this interleaved reference scan prolongs the release time and therefore allows the full recovery of MRI signal(blue line) compared with referenceless inversion recovery acquisition(red line)

recovery T1 weighted acquisition. TI was optimized that the signal is above zero at TI of reference image for all tissues. As is shown in Figure 1.4, the reference phase was removed from the T1 weighted image and produces the phase sensitive image.

To minimize the motion between the T1 weighted image and reference image, two scans are usually interleaved (Figure 1.4)[6, 8]. In addition to motion minimization, compared with referenceless inversion recovery acquisition(red line, Figure 1.4), an extra non-inversion scan inserted between the two inversion-recovery scans allows the full recovery of magnetization signal (blue line, Figure 1.4)and therefore increases the SNR and contrast of tissues. PSIR principle has been applied to cardiovascular disease, including myocardial LGE scar imaging [6] and cerebrovascular atherosclerosis imaging[8]. With the fully sampled reference scan, however, the total scan time is doubled. Besides, the reference image may introduce artifacts

to the reconstructed phase sensitive images.

1.3 Cardiovascular disease

Cardiovascular diseases include the diseases of heart, vessel wall and the related vascular diseases in the brain. Cardiovascular diseases are the leading cause of death and disabilities in the United States[9]. Atherosclerotic vascular diseases are the major type of cardiovascular disease and are caused by the progress of atherosclerosis. Atherosclerotic vascular disease can be categorized into coronary heart disease and cerebrovascular disease.

Atherosclerosis usually exists within the vessel wall of medium or large sized arteries[10]. It may start to develop from very young age. During its progress, fatty materials and cholesterols gradually accumulate inside the vessel wall and finally develop into plaque[11]. The harm of atherosclerosis plaque includes the irregular lumen boundary, narrowed lumen size and the reduced elasticity of muscles in the vessel wall[12]. Among the atherosclerosis plaques, those with unstable structure and constituents are more vulnerable to rupture and formation of thrombus than the 'stable' plaques[13]. Blood clots developed from thrombus may flow along the arteries and block the small branches of arteries. The supply of oxygen and nutrients to the surrounding tissues will be reduced or even stopped around the blocked arteries which may lead to the death of tissues[12]. It will cause stroke if the blockage happens in the brain and myocardial infarction if it happens in the heart [12]. In 2008, around 17.3million death were caused by the cardiovascular disease and among them, 7.3 million (42%) were caused by heart attack while 6.2 million (36%) were caused by stroke[14]. Therefore, the ability to separate the patients with vulnerable atherosclerosis plaque and observe the development of symptom non-invasively will be of importance to improve the life quality and reduce the cost burden of the patients and their families.

1.4 Myocardial infarction and its diagnosis with phase sensitive imaging

Myocardial infarction is a serious disease triggered by the rupture of atherosclerotic plaque within the coronary artery. If the coronary is clotted too long, the shortage of blood will

lead to the death of myocardial cells and the development of collagen scar. This process is called ischemic cascade and is irreversible[15]. The development of myocardial scar not just damages the heart permanently, it also exposes the patients to the risk of arrhythmias and development of ventricular aneurysm, both of which are life threatening. Besides, for the heart with the myocardial scar, the blood pressure may drop to a very dangerous level which may trigger new coronary ischemia and myocardial infarction[15]. Therefore, the ability to detect and quantify the myocardial scar accurately is important to prevent the second event of myocardial infarction to the patients.

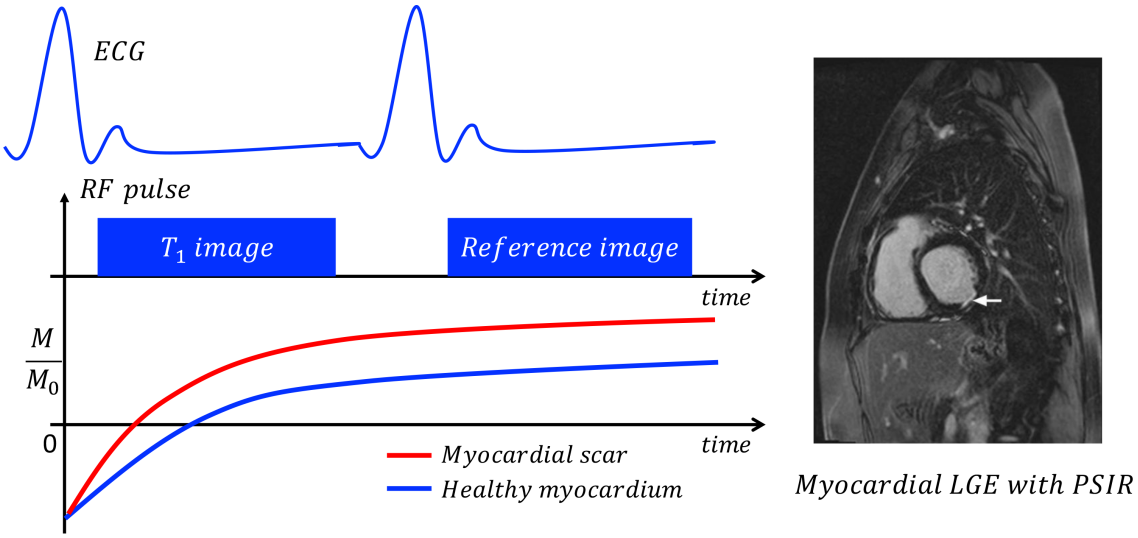

Figure 1.5: Design of PSIR sequence. The ECG signal is used to trigger the acquisition of both the inversion recovery T1 weighted image and the reference image. The two images are interleaved to reduce the motion between scans. The inversion RF pulse is applied every other heartbeat. The figure on the right side is the example of myocardial LGE image. The LGE enhanced signal is in the inferolateral wall which represents a small post-ischemic sub-endocardial scar [16].

Currently, myocardial late gadolinium enhancement (LGE) imaging is the major MRI tool for myocardial scar detection and quantification. This method needs the administration of contrast agent, which has relatively short T1, and the fibrous tissues like scar have slower washout rate than surrounding healthy tissues. Waiting a short period of time (typically

10-30 minutes) after injecting the contrast agents [16], much more contrast agent remains in the scar than the surrounding healthy tissues and in the T1 weighted image, myocardial scar shows hyperintense signal relative to the healthy muscles (Figure 1.5[16]).

As mentioned previously, PSIR with a fully sampled reference scan is often used with myocardial LGE to further enhance the scar/myocardium contrast. Inherited from the conventional myocardial LGE acquisition scheme, a scout scan is usually used to determine the optimal TI that null the myocardial signal[16]. *For PSIR, a fully sampled reference scan doubles the scan time compared with conventional inversion recovery acquisition and thereby limiting its clinical application for time-intensive 3D whole heart imaging. 3D whole heart phase sensitive LGE imaging has been shown to increase the sensitivity of myocardial scar detection while having greater spatial coverage and resolution, as well as higher signal to noise ratio (SNR)[17, 18]. Furthermore, the large field of view(FOV) of 3D Myocardial LGE image covers the region with complex structure, components and SNR distribution, which may induce susceptibility related local B_0 inhomogeneity. During 3D acquisition, in addition to the susceptibility related local B_0 inhomogeneity, motion between reference scan and inversion recovery scan may introduce artifacts in the reconstructed phase sensitive.*

1.5 Stroke

Stroke, which is also known as cerebrovascular accident (CVA), is the death of tissue in the brain caused by the shortage of blood supply. Stroke currently is the fourth leading cause of death in the United States [19]. Each year about 795,000 people in the United States suffered at least one stroke [14] and the lifetime risk of stroke is around 1 of every 6 people[20]. There are two major categories of strokes: ischemic stroke is caused by the insufficient blood supply and hemorrhagic stroke is caused by the leakage of blood from the brain vessels [21]. Of all the strokes cases, 87% are ischemic stroke while the rest are hemorrhagic stroke[22]. As to the ischemic strokes, there are also two major categories: cerebral thrombosis and cerebral embolism [23]. Cerebral thrombosis represents the cases that the thrombus developed right at the clotted part of vessel and cerebral embolism describes the cases that the location

of thrombus development is different from the location of the clotted vessel. For cerebral embolism, thrombus usually develope at the large arteries such as aorta and carotid arteries [24]. Therefore, to prevent the development of stroke, especially cerebral embolism, it's important to place the arteries vulnerable to develop the high-risk atherosclerosis plaques, under close watch. Besides, for the patients with asymptomatic plaques, it's also important is to separate the high-risk plaques, which are vulnerable to rupture and develop into thrombus, from those that are relatively stable. MRI is a valuable tool to evaluate the components of plaques.

1.6 Risk factors of atherosclerosis plaque

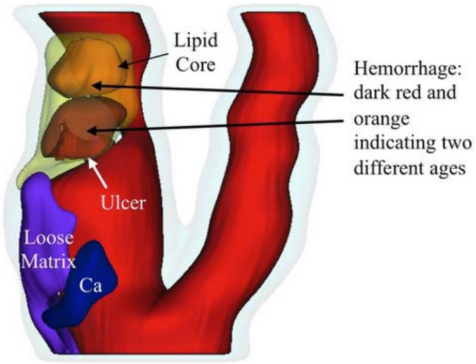

Figure 1.6: Atherosclerosis plaque which contains lipid-rich necrotic core (LRNC), fibrous cap, calcification and intraplaque hemorrhage (IPH)

Atherosclerosis plaques have complex composition (Figure 1.6[10]). In this section, four risk factors which have strong correlation with high-risk plaque will be introduced.

1.6.1 Luminal stenosis

Arterial luminal stenosis may change or even block the blood flow. Currently, it's the major clinical metric to differentiate the high-risk atherosclerosis plaques. Surgery is usually

suggested to the patients with stenosis degree higher than 70%[25]. The luminal stenosis is believed to change the shear stress and increase the risk of thrombosis development. Besides, the existence of severe stenosis may also indicate the existence of atherosclerosis plaques at other locations [26].

1.6.2 Lipid-rich necrotic core and fibrous cap(LRNC)

LRNC is a well-delineated region within the intima and is a mixture of components such as cholesterol esters, free cholesterol, phospholipids, triglycerides, inflammatory cells, red blood cells and fragments of an extracellular matrix [26, 27]. LRNC is usually covered by fibrous cap - a layer of connective tissues consisting of macrophages and smooth muscle cells[28]. Histological studies suggested that LRNC with thin fibrous cap predicts a higher risk to the formation of thrombus [29].

1.6.3 Intraplaque hemorrhage (IPH)

IPH is caused by neo-capillary rupture [30, 31]. Previous research shows that plaques with 50%-79% stenosis have a more significant change in LRNC containing IPH than those without IPH [32] and neo-vessel density is positively correlated with the progression of LRNC formation [33, 34]. Possible explanation is that red cell membrane is 1.5-2 times richer in cholesterol [13, 35] relative to other cells and cholesterol is a key component of LNRC. Therefore, plaques with IPH usually have a higher hazard ratio(HR) for ischemic cerebrovascular events compared with those without IPH [26, 27].

1.6.4 Calcification

Coronary artery calcium score (CACS) is an important metric to predict cardiac ischemic events [36]. The role of calcification is not straightforward for stroke. Big chunk of calcification distant from thick fibrous cap usually predicts a stable plaque [37] while calcified nodules near or within a thin fibrous cap usually predict vulnerable plaques [13, 26].

Table 1.1: Hazard ratio of atherosclerosis risk factors based on the literature review

Components name	HR
IPH	4.59 (95% CI: 2.91-7.24)
LNRC	3.00 (95% CI: 1.51-5.95)
Thinning/rupture of fibrous cap	5.93 (95% CI: 2.65-13.20)
Stenosis	1.03 (95% CI: 1.01-1.04)

1.6.5 Hazard ratio of risk factors

Luminal stenosis is the major clinical metric to evaluate the risk of atherosclerosis plaques [38, 39]. The hazard ratio of IPH, LNRC and thinning/rupture of fibrous cap is summarized based on the literature review of nine studies totally including 779 samples [39]. The HR of stenosis was summarized from a prospective cohort study and stenosis degree is a continuous variable[40]. HR of these risk factors are shown in Table 1.1.

Table 1.1 shows that both IPH and LNRC are factors that can significantly increase the risk of atherosclerosis plaques. Considering the connection between IPH and LNRC, the ability to detect IPH is valuable to evaluate plaque vulnerability.

1.6.6 Stenosis vs. Model including multiple risk factors

Previous research shows that stenosis itself cannot reliable predict stroke risk of atherosclerosis plaques in symptomatic patients with stenosis $< 70\%$ [41] and asymptomatic patients with all degrees of stenoses[42].Risk factors like IPH can help better predict the stroke events. Efforts have been made to use the model that including multiple features to better predict the clinical outcomes[43].

1.7 MRI of risk factors of atherosclerosis plaques

1.7.1 Multi-contrast atherosclerosis MRI

MRI can differentiate tissues through multiple contrast weighting and has been used to detect risk factors of atherosclerosis plaque. Below is the introduction of major related MRI techniques.

1.7.2 Luminal stenosis

Digital subtraction angiography (DSA) is the current gold standard to access the luminal stenosis[44] of carotid artery. DSA, however, is invasive and involves ionizing radiation. Contrast enhanced MRA (CE-MRA) and time of flight (TOF) are the alternative MRI approaches to DSA. With maximum intensity projection (MIP) from CE-MRA or TOF images, luminal stenosis can be quantified using North American symptomatic carotid endarterectomy trial(NASCET) standard[44, 45] .

1.7.3 Calcification

Calcification cannot produce MRI signal and therefore has hypointense signal in MRI images. To detect the calcified nodules that protrude into the lumen, bright blood or grey blood MRA is preferred.

1.7.4 LRNC

LRNC is usually detected using contrast enhanced T1W MRI, and the LRNC usually shows a hypointense signal relative to adjacent fibrous tissue due to the reduction or absence of contrast agents[46].

1.7.5 IPH

Intraplaque hemorrhage usually degrades into methemoglobin with shortened T1[47]. Therefore, IPH has hyperintense signal in T1 weighted images [8, 26]. Magnetization-prepared rapid gradient echo (MP-RAGE)[48] is often used for IPH detection. An inversion recovery RF pulse is used to introduce T1 weighting to MP-RAGE images[48].

1.7.6 Summary

To detect multiple risk factors of atherosclerosis plaque, several MRI protocols with different contrast weighting are needed. This scheme has several problems. First, only MRA is allowed for clinical test of atherosclerosis by the insurance companies in the United States. Second, compared with MRA, the multi-sequence MRI scheme requires extra training and work, like FOV selection and parameters optimization for the physicians. Third, this procedure inevitably prolongs the total scan time and therefore increases the scan cost. Lastly, this scheme is sensitive to mis-registration caused by motion between scans. Therefore, multi-contrast, multi-scan MRI scheme needs to be simplified for clinical application.

1.8 Phase sensitive reconstruction for atherosclerosis imaging (SNAP)

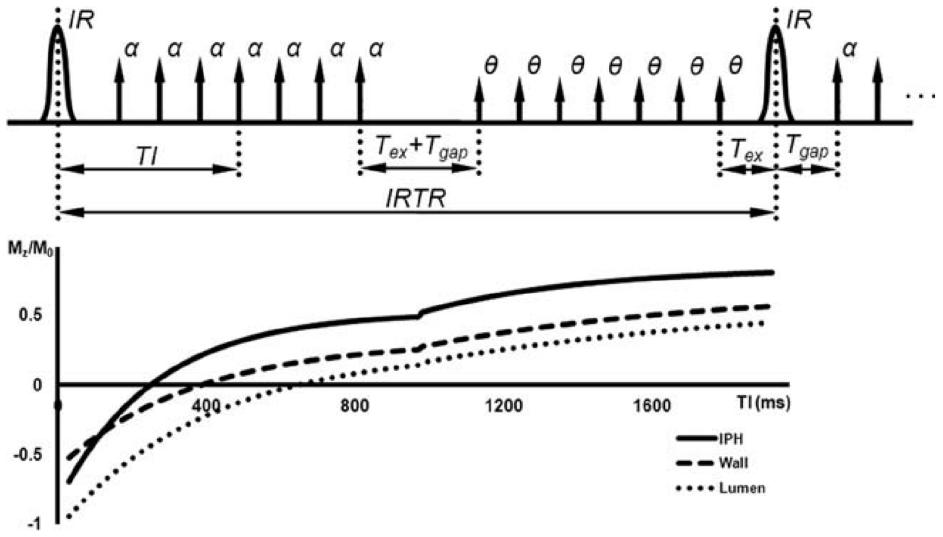

Figure 1.7: The sequence design of SNAP and the release trajectory of IPH, vessel wall and lumen during SNAP scan.

Based on the PSIR method, simultaneous noncontrast angiography and intraplaque hemorrhage (SNAP)[8] imaging was developed for simultaneous detection and quantification of luminal stenosis and IPH within the cerebrovascular arteries. SNAP also uses a fully sampled reference scan to reconstruct the phase sensitive image. The design of SNAP sequence is shown in Figure 1.7 [8].

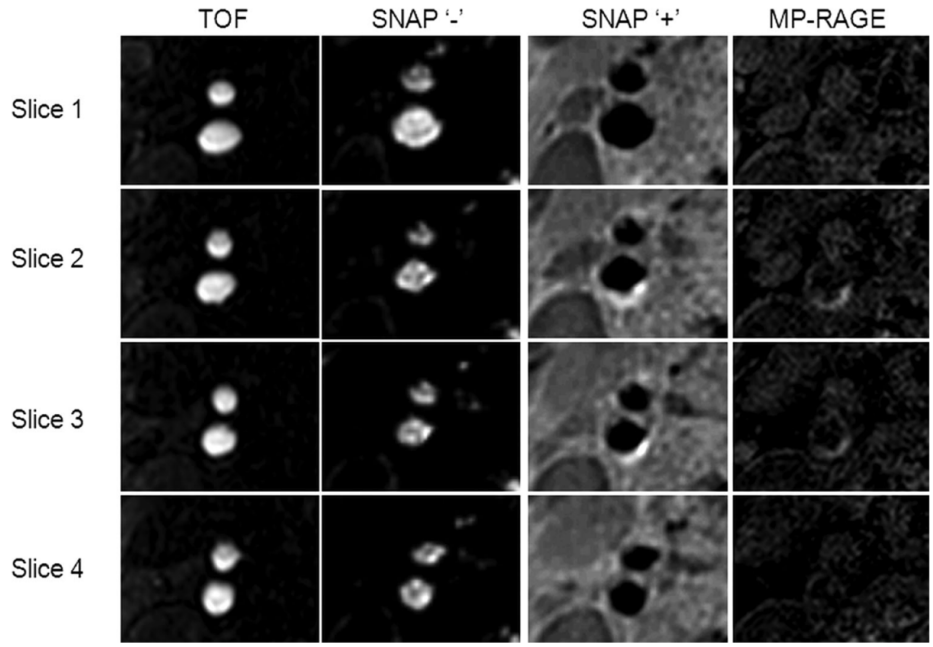

Figure 1.8: Demonstration of the slices from two patients scanned with TOF, SNAP and MP-RAGE. The lumen, the negative part of SNAP MRA, is consistent with TOF while the IPH in SNAP image shows a higher contrast than MP-RAGE.

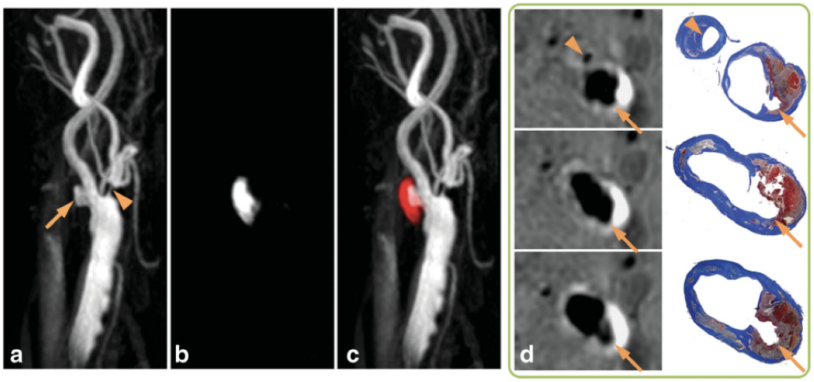

Figure 1.9: MIP image of lumen(a) and IPH(b) and joint view of lumen and IPH(c). These figures demonstrate the flexibility of SNAP to access different risk factors. Comparison between SNAP and Mallory's trichrome histology slides (d) confirms the delineation of lumen and IPH with SNAP.

The IPH has relative short T1(500 ms) [49] compared with vessel wall and blood (1115

ms and 1550 ms respectively[50]). As can be seen from Figure 1.7, after repeated inversion recovery RF pulses, the magnetization of IPH and vessel wall, both of which are static tissues, is partially saturated while that of blood is not influenced due to its full refreshment. The parameters of SNAP were optimized so that 1) at TI, when the optimal contrast between tissues are achieved , the signal of IPH and lumen(blood) is positive and negative respectively and the signal of vessel wall is around zero; 2) the contrast of IPH/vessel wall and vessel wall/lumen are maximized. Figure 1.8 [8]& Figure 1.9 [8] demonstrate that with the polarity map of SNAP, IPH and luminal stenosis can be accessed either together or separately.

Compared with scheme that requires multiple MRI scans, SNAP has several advantages. First, as a phase sensitive method, assisted by the polarity map, its dynamic range of contrast is doubled. Second, with the polarity contrast, SNAP can simultaneously detect and quantify two major risk factors (IPH and luminal stenosis) both of which are naturally registered. Third, compared with TOF, which relies on flow refreshment to produce lumen contrast, lumen contrast of SNAP MRA relies on T1 weighting and therefore have a larger coverage and is less sensitive to flow artifacts.

Similar with PSIR, the fully sampled reference scan of SNAP doubles the scan time and only the phase of the reference image is used to help reconstruct the phase sensitive image. The magnitude part, which is PD weighted with high SNR, can be used to detect other risk features like calcification. Besides, only the magnitude/intensity contrast instead of binary polarity contrast is used to identify the tissue boundary of SNAP and therefore and the polarity feature is not fully used. Furthermore, SNAP can not separate the arteries from veins.

1.9 Research goal and hypothesis of this study

Phase sensitive images are of great value for cardiovascular disease because 1) the dynamic range of contrast is doubled compared with conventional inversion recovery image, and 2) multiple risk factors can be simultaneously detected aided by polarity contrast. The fully sampled reference scan required by conventional phase sensitive reconstruction, however, double the scan time and only the phase part of reference image is used. Furthermore,

polarity contrast of phase sensitive image is not fully used yet. Motivated by these issues, the goals of this thesis can be summarized as:

- Directly reconstruct the phase sensitive image without reference scan.
- Evaluate the accuracy of tissue boundary identified by the polarity contrast.
- Optimize SNAP for venous flow suppression and calcification detection using the reference image.

The hypothesis of this study is that the imaging efficiency and capability of conventional phase sensitive reconstruction can be improved either through removing the reference scan or exploring more features from both the phase sensitive image and the reference image. Based on this hypothesis, the specific aims of this project are:

Specific Aim 1: Directly reconstruct the phase sensitive image without reference scan

a Develop the algorithm to directly reconstruct the phase sensitive image fast and reliably.

b Validate the developed method against PSIR reconstruction with myocardial LGE images.

Specific Aim 2: Identify the components of interest(lumen) with optimized phase sensitive MRI:

a Identify the lumen contour based on negative polarity of SNAP MRA on the carotid arteries with stenosis.

b Evaluated the lumen area and percent stenosis identified by the negative polarity of SNAP MRA using CE-MRA as the reference

Specific Aim 3: Improve SNAP for calcified nodules detection and artery/vein separation assisted by the binary polarity map

a Transfer the lumen contour from SNAP MRA on the magnitude of reference image to produce the grey-blood PD weighted images for calcified nodules detection.

b Enable SNAP to saperate arteries and veins.

Upon the competition of this study, the phase sensitive reconstruction can be optimized in three aspects: First, the referenceless phase sensitive reconstruction method can halve the scan time of conventional PSIR, potentially allowing large coverage 3D myocardial imaging. Besides, referenceless acquisition can avoid the artifacts transferred from the reference image. Second, negative polarity can be used directly to identify the lumen boundary. More importantly, this study demonstrated the potential of using polarity map of phase sensitive image to identify other risk factors like myocardial scar. Third, in addition to IPH and luminal stenosis, calcified nodules near thin fibrous cap can be detected with SNAP and arteries can be separated from veins.

Chapter 2

SPECIFIC AIM 1: 3D TRUE PHASE POLARITY RECOVERY WITH INDEPENDENT PHASE ESTIMATION USING THE THREE-LAYER STACKS BASED REGION-GROWING (3D-TRIPS)

2.1 Background and study goal

As discussed in Chapter 1, myocardial LGE with PSIR [51, 52, 53] has been used to identify myocardial scar [6]. The fully sampled reference scan required by PSIR, however, doubles the scan time and therefore restricts its clinical application for 3D whole heart imaging. Compared with 2D imaging, 3D whole heart LGE imaging has the improved sensitivity for scar detection thanks to its larger coverage, higher SNR and resolution [17, 18].

The acquisition time of phase sensitive image can be reduced if it is directly reconstructed using the inversion recovery complex image without the reference scan[4]. This is, however, prevented by the background phase [4, 8, 54], and the phase of inversion-recovery image usually deviates from the true phase. Therefore, for direct phase sensitive reconstruction, post-processing is needed to remove the background phase. In this section, 3D True Phase Polarity Recovery with Independent Phase Estimation Using Three-layer Stacks based Region-growing (3D-TRIPS) was developed to directly reconstruct the 3D phase sensitive images simply using the raw complex inversion recovery T1 weighted images. This method was evaluated on 15 subjects using PSIR images as the reference standard.

2.2 Established direct phase sensitive reconstruction methods

Efforts have been made on referenceless phase sensitive reconstruction. Before the introduction of the method developed in this study, two existed referenceless phase sensitive

reconstruction methods developed by Xiang[54] and Wang[4] will be introduced first.

2.2.1 Multi-seed region growing spin reversal(RGSR) [54]

RGSR uses region-growing and was developed before PSIR. It hypothesizes that the background phase is spatially smooth. After normalizing each complex vector in the image, starting from the seed voxel, each of its neighboring voxels is evaluated with:$|A| = |N_x * N_y|$, where the background phase of N_y is known and N_x is the neighboring voxel of N_y, whose background phase is unknown. Because both N_y and N_x are normalized vectors, $|A|$ is equivalent to $cos\theta$, where θ is the angle between N_y and N_x. A large $|A|(> 0.96)$ means a small angle$(< 16.36^o)$ between the background phase of N_y and N_x. Two vectors with large $|A|$ will be regarded as qualified voxels for background phase estimation. If $A > 0$, phase of N_x is regarded as the background phase. Otherwise, phase of $-N_x$ is the background phase. After that, N_x will be marked as processed voxels and its neighboring voxels will be processed based on the above rules with region-growing. RGSR stops when all the qualified voxels are processed.

The problem with RGSR is that, the background phase of only one neighboring voxel is used as reference for each voxel. RGSR is therefore sensitive to the noise especially in the region with low SNR. For RGSR, only voxels with small background phase difference are regarded as qualified voxels which limits its application to myocardial imaging where myocardium has low SNR.

2.2.2 Referenceless acquisition of phase-sensitive inversion-recovery with decisive reconstruction (RAPID) [4]

Similar with RGSR, RAPID also uses region-growing. A small region with high SNR is selected as the seed region and a mask $M_{processed}$is used to mark the processed voxels. The improvement of RAPID relative to RGSR is that, the average background phase of multiple neighboring voxels instead of one voxel is used as the reference. Therefore, RAPID can cover the relative low SNR region for background phase estimation. To prevent the error

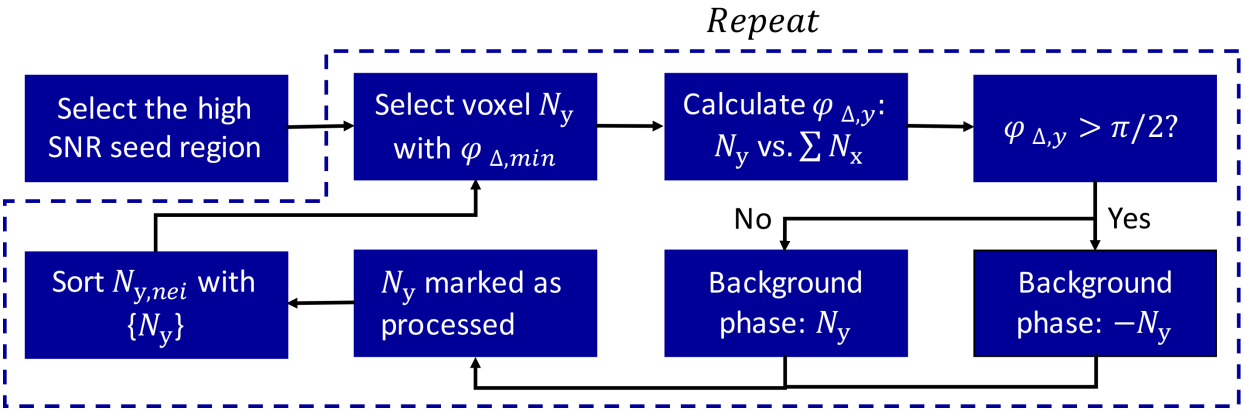

Figure 2.1: Flow chart of RAPID algorithm

transferred from noisy voxels to good voxels, region-growing track is optimized based on the neighboring phase difference φ_Δ. φ_Δ is defined as the angle between the target voxel and the average of neighboring background phase. During region growing, unprocessed voxel with minimum φ_Δ will be processed first and region growing stops when all the voxels are processed. The flow chart and example of RAPID are shown in Figure 2.1 and Figure 2.2[4]:

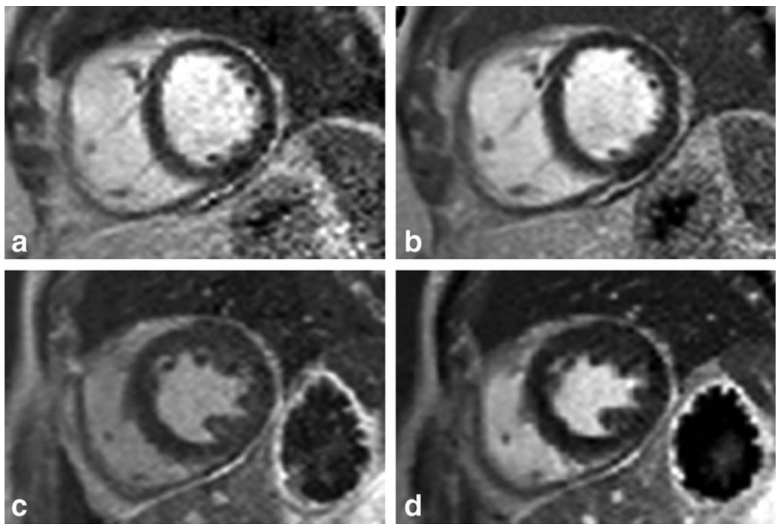

Figure 2.2: 2D Myocardial LGE images reconstructed with RAPID(a,c) and PSIR(b,d) from two subjects. Good consistency was achieved between the two reconstruction methods

Problems of RAPID

RAPID, has several problems:

First, RAPID is slow. After processing one voxel, the phase difference of its unprocessed neighboring voxels needs to be recalculated and sorted along with other unprocessed voxels. The time complexity of major sorting algorithm is $O(n^2)$ or $O(nlogn)$, where n is related to the total number of image voxels. The computation time increases fast with image size and therefore is not feasible for large coverage, high-resolution 3D reconstruction.

Second, high SNR voxels with negative polarity or in the polarity transition region have a lower priority relative to low SNR voxels with smaller phase difference. The high SNR voxels therefore are sensitive to the error transferred from the low SNR voxels. Furthermore, each of the negative voxels will be visited multiple times during region-growing, due to its low priority , which further prolongs the computation time.

Third, the model of RAPID and other phase based region-growing optimization methods did not take into consideration the preexisted phase difference and the polarity of phase difference.

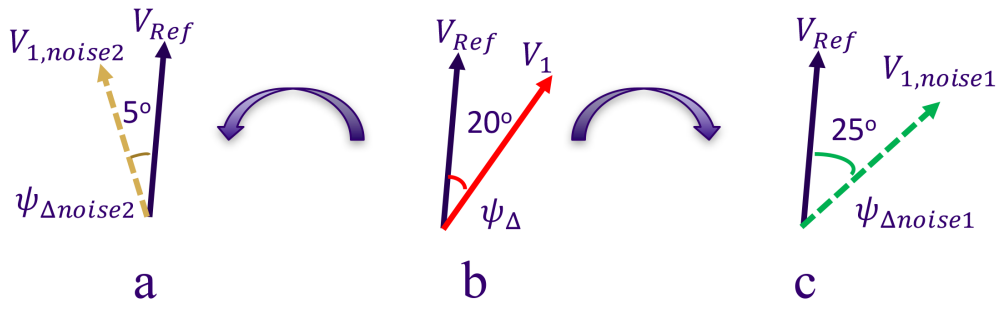

Figure 2.3: (b) shows the angle(20^o) between a vector V_1 and its reference background phase and no noise was added to V_1. After adding noise to V_1, the angle between two vectors changed to 5^o(a) for $V_{1,noise2}$ and 25^o for $V_{1,noise1}$(b)

As demonstrated in Figure 2.3, there is a preexisted phase difference(20^o) between voxel V_1 and its reference vector V_{ref}. This reference vector can either be a single neighboring voxel of RGSR or the average of several neighboring voxels with RAPID. Then two noise vectors were added to V_1, and the phase difference changed to -5^o with $V_{1,noise2}$ and 25^o with $V_{1,noise1}$. RAPID region-growing will prioritize $V_{1,noise2}$ over $V_{1,noise1}$ because of its smaller absolute phase difference while $V_{1,noise1}$ has a smaller noise than $V_{1,noise2}$. This problem means that with conventional phase based region growing used by RAPID, high-SNR voxels are sensitive to the error transferred from the low-SNR voxels.

2.2.3 Summary

For robust true phase reconstruction, current referenceless phase sensitive reconstruction methods either require a large continuous high SNR region [55], human supervision [54, 55], prior knowledge of polarity distribution [54], or long computation time [4]. *For 3D myocardium LGE imaging, the true phase map has complex anatomical structures and the high SNR regions (e.g., left ventricular blood pool) are separated by low SNR regions (e.g., normal myocardium). The existing referenless phase sensitive reconstruction methods [8, 54, 55]are still vulnerable to problem that the error may be transferred from low SNR/ noisy voxels to good ones. And the error may be transferred to large regions. Therefore, a fast and*

robust direct phase sensitive reconstruction method is needed for 3D whole heart myocardial LGE imaging.

2.3 3D-TRIPS

As discussed in the previous session, the key for direct background phase estimation is the optimization of region-growing track so as to limit or delay the error transferred from the low SNR voxels to high SNR ones. In the following section, 3D True Phase Polarity Recovery with Independent Phase Estimation Using Three-tier Stacks Based Region-growing (3D-TRIPS) was introduced which optimizes the region-growing track based on the SNR/signal intensity.

2.3.1 Principle of direct phase sensitive reconstruction

Influence of SNR on background phase estimation

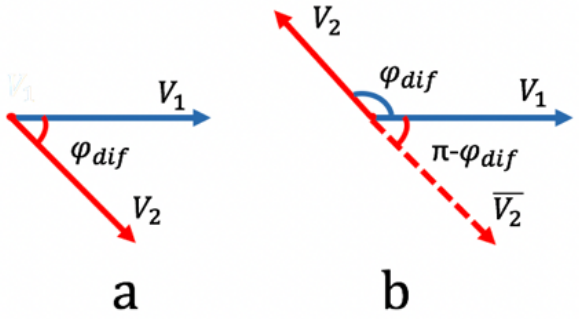

Figure 2.4: a) Two neighboring vectors V_1, V_2 with phase difference $\varphi_{dif} \leq \pi/2$ b) Two neighboring vectorsV_1, V_2, with phase difference $\varphi_{dif} > \pi/2$, and the phase difference between V_1 and conjugate of V_2 is smaller than $\pi/2$

As demonstrated in Equation 1.1, noise has a great impact on the background phase of the low SNR voxels. Like RGSR and RAPID, major referenceless phase sensitive reconstruction methods hypothesize that the background phase is spatially smooth within the FOV [54, 4]

which means that in the background phase map, the angle between neighboring voxels with reasonable SNR should be smaller than $\pi/2$. During region-growing, as is shown in Figure 2.4, if the angle φ_{dif} between a target voxel and the average of neighboring voxels (neighboring voxel in RGSR method) is smaller than $\pi/2$ (Figure 2.4a), phase of target voxel φ_z is the background phase, otherwise, $\pi - \varphi_z$ is the background phase (Figure 2.4b)

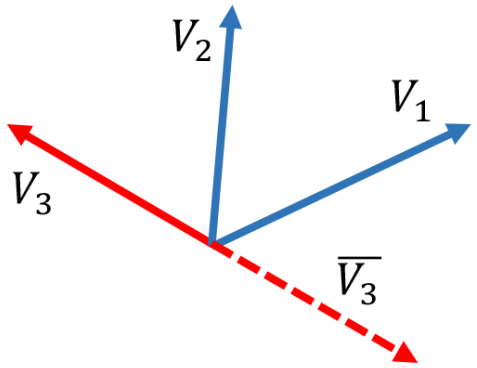

Figure 2.5: Vectors of three neighboring voxels V_1, V_2 and V_3. The angle between V_1 and V_2, V_2 and V_3 are both $\pi/3$. Phase of V_1 and V_2 are the background phase. Neither V_3 nor its conjugate satisfy that its angles relative to V_1 and V_2 are both smaller than $\pi/2$

The above assumption, however, does not apply to the low SNR regions because of the problem of indeterminate background phase. The angle between V_1 and V_2, V_2 and V_3 are both $\pi/3$ respectively (Figure 2.5). Suppose that the phases of V_1 and V_2 are the background phase and the background phase of V_3 is to be determined. As shown in Figure 2.5, neither V_3 nor its conjugate can fulfill the assumption that their angles with V_1 and V_2 are both acute angles. With RAPID region-growing, either V_3 or its conjugate may be regarded as the background phase. Using the average phase of neighboring voxels may mitigate this problem but cannot solve it completely. Furthermore, the existence of indeterminate background phase may lead to the polarity error in the distant region.

Monte-Carlo simulation

To study the relation between SNR and background phase estimation, in this study, two assumptions were proposed:

Assumption 1: Using region-growing, probability with indeterminate background phase inversely correlates with SNR.

Assumption 2: Prioritizing the high-SNR voxels can improve the background phase estimation of low-SNR voxels.

Monte-Carlo simulation was used to test these two assumptions. For Assumption 1, a 3D structure containing $2 \times 2 \times 3$ voxels with the same initial positive signal was used. Complex Gaussian noise with the same standard deviation was added to each voxel with SNR ranging from 0 to 10. Background phase was then calculated voxel-by-voxel using region-growing. For each SNR, 10000 simulations were performed. For the ith simulation, $r_{i,SNR}$ was recorded as 1 if there was indeterminate background phase, otherwise $r_{i,SNR}$ was recorded as 0. For each SNR value, the average of indeterminate background phase ratio was calculated as: $r_{SNR} = \sum r_{i,SNR}/10000$.

For Assumption 2, two groups of voxels were involved in the simulation. The structure of the first group was the same as that of the previous simulation. The second group contained $2 \times 2 \times 4$ voxels. Unlike the first group, the initial intensity of the first four voxels in the second group was ten times that of the remaining 12 voxels. During this simulation, complex Gaussian noise with the same standard deviation was added to the two groups of voxels with SNR of the low intensity signals ranging from 0 to 10. During region-growing, background phase of the four voxels with higher intensity were calculated first. For each SNR, 10000 simulation rounds was performed, and for each simulation round the error ratio was calculated as: $r_{i,SNR} = N_p/N$ where $N_p$represents the number of voxels with incorrect polarity. N represents the total number of voxels with low intensity and is 12 in this study. Average error ratio was given by: $r_{SNR} = \sum r_{i,SNR}/10000$.

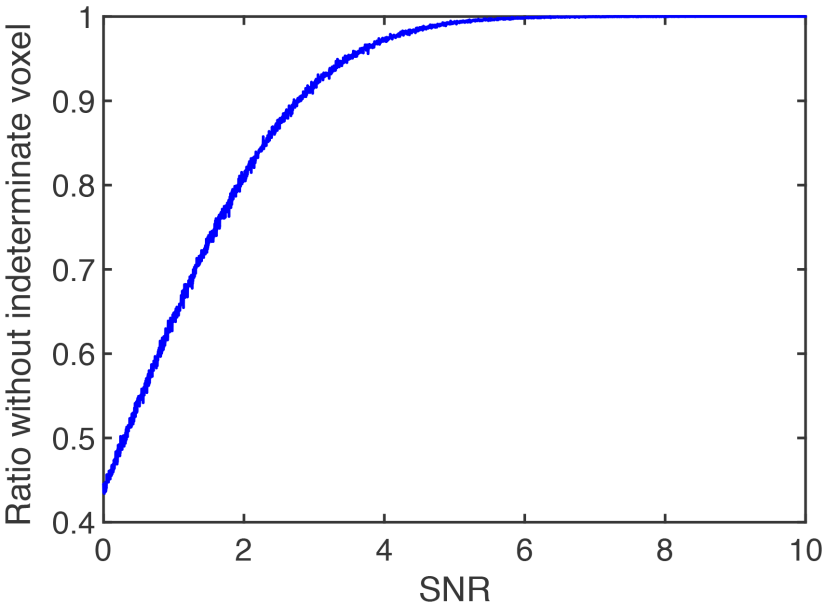

Figure 2.6: Monte Carlo simulation of the probability of indeterminate voxels vs. SNR when estimating background phase with region growing. This figure shows that the probability of no indeterminate voxels is 100% when SNR is high and drops sharply when SNR is smaller than 5.

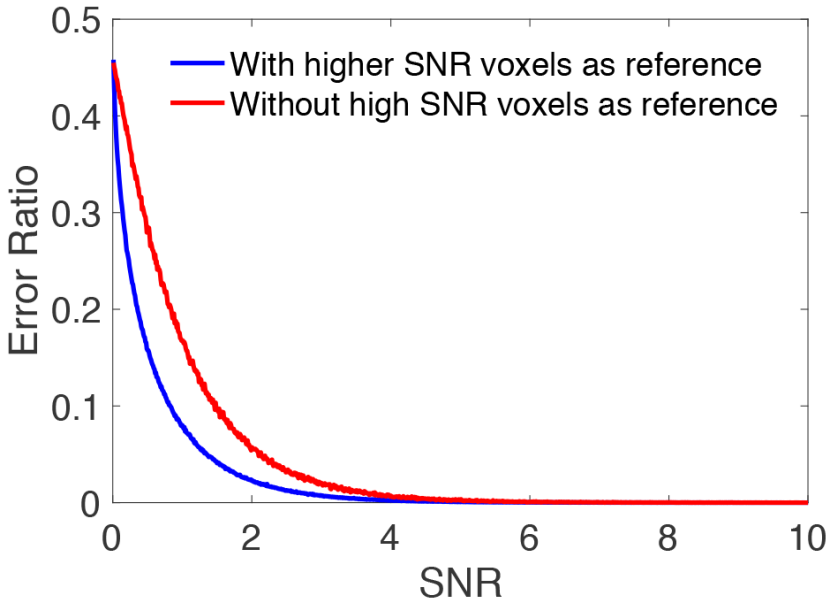

Figure 2.7: Error ratio vs. SNR through Monte Carlo simulation of background phase calculation. The red line is the simulation result without higher SNR voxels as the reference. It shows that when SNR is small, the error ratio negatively correlates with SNR and when SNR is near zero, the background phase is almost randomly identified. The blue line is the result of simulation with higher SNR voxels as the reference. A comparison between the two lines shows that if the high SNR voxels are processed first and used as the reference for low SNR voxels, the error ratio drops significantly.

Simulation results

The simulation results for the two assumptions were shown in Figure 2.6 and Figure 2.7. As can be seen in Figure 2.6, the ratio with indeterminate phase negatively correlates with SNR. Figure 2.7 shows that when the SNR is high (≥ 5), the background phase can be reliably estimated, but when SNR is lower than 5, r_{SNR} drops sharply. For voxels with SNR< 1, both the error ratio and the probability of indeterminate voxels are very high.

The comparison between the background phase estimation with and without high-SNR reference demonstrates that if the high SNR voxels are calculated first and used as reference for the low SNR voxels, the error rate can be reduced compared with simply relying on the neighboring low SNR voxels.

2.3.2 3D-TRIPS

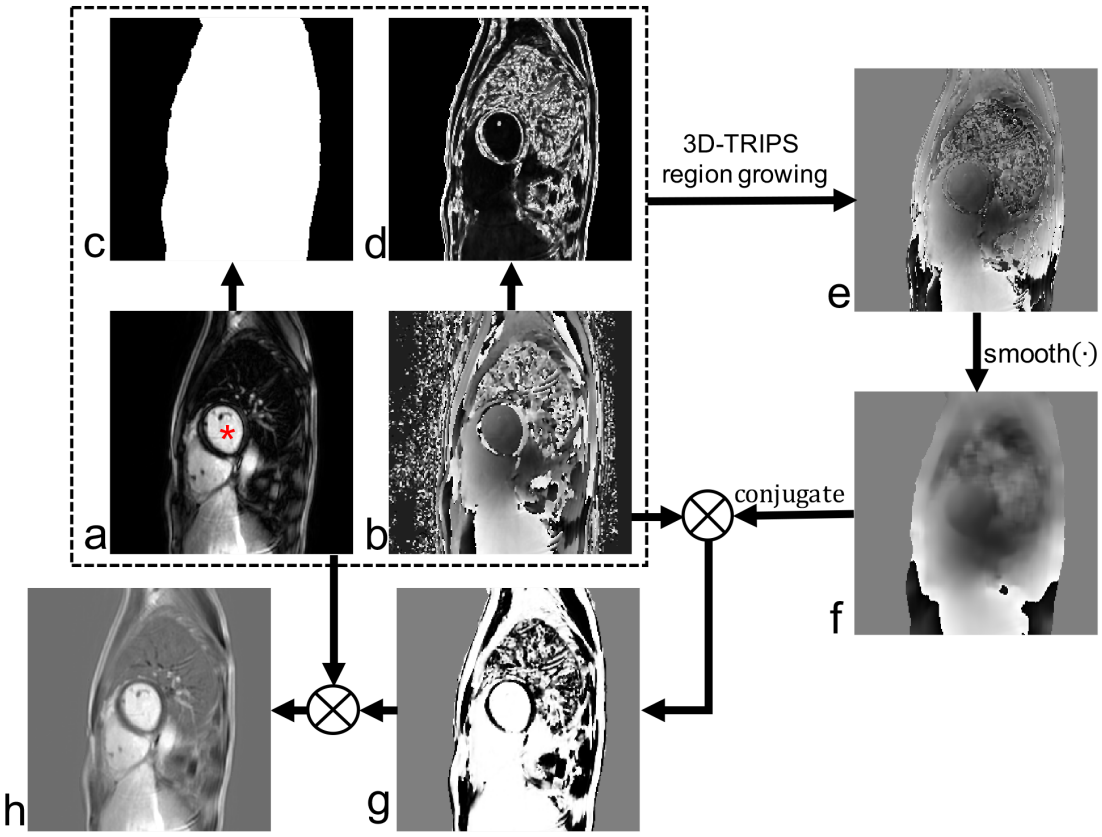

Figure 2.8: Flow chart for 3D-TRIPS: (a) is the magnitude of the T1 weighted image and the red " $*$ "marks the seed point of region-growing, (b) is the phase image, (c) is the mask M_{global} calculated from (a), (d) is the maximum neighboring phase difference map M_{global}, (e) is the background phase calculated with the proposed 3D-TRIPS method, (f) is the smoothed background phase map, (g) is the polarity map, and (h) is the final phase sensitive image.

Based on the two assumptions, 3D-TRIPS uses signal intensity, which positively correlates with SNR, to evaluate the reliability of voxels for background phase calculation. In addition, because the high SNR voxels in the polarity transition region have large phase difference, 3D-TRIPS uses the maximum neighboring phase difference to assist the separation of region with different priority during region-growing.3D-TRIPS is described below and its flow chart

is shown in Figure 2.8:

Step 1: Two matrixes are calculated: A 3D binary mask M_{global}(Figure 2.8c) is used to exclude the low SNR background signal and a 3D matrix P_{dif} , is used to record the maximum phase difference $\varphi_{dif,z}$ relative to the neighboring voxels:

$$\varphi_{dif,z} = max(|angle(C_z \times conj(C_{z+(m,n,l)}))|), m, n, l \in (-1, 0, +1), |m| + |n| + |l| = 1 \quad (2.1)$$

where C_z represents the complex signal of the inversion recovery image and $C_{z+(m,n,l)}$ represents its six neighboring voxels , $|angle(*)|$ and $conj(*)$represent the absolute phase and conjugate of a complex voxel respectively.

Step 2: Calculate the background phase map I_{BPS} using 3D-TRIPS region-growing. During region-growing, $M_{processed}$ records the voxels that have been processed. A voxel from the blood pool of left ventricle with high SNR is selected as the seed. A structure with three-layer grouped stacks is then used to optimize the region growing track. The phase difference between a voxel and the average of its neighboring background phase is calculated as:

$$\phi_{dif,z} = |angle(C_z \times conj(C_{average}))|, C_{average} = mean([M_{global} M_{processed} M_{local}] I_{BPS}) \quad (2.2)$$

M_{local} is a binary mask which selects the neighboring voxels of C_Z. In this study, the size of M_{local} is 1/15 of the size of the 3D image. If $\phi \leq \pi/2$, C_Z is added to I_{BPS} otherwise $-C_Z$ is added to I_{BPS}. The unprocessed neighboring voxels of I_{BPS} are then pushed into the stacks. The region-growing stops when all the stacks are empty.

Step 3: The calculated background phase map of I_{BPS} is smoothed to I_{SBPS} using a low pass filter.

Step 4: Similar to PSIR, the phase sensitive image I_{PS} was calculated as:

$$I_{PS} = real(I_{raw} \times conj(I_{SBPS})/|I_{SBPS}|) \quad (2.3)$$

Where $real()$ represents the real part of a complex value.

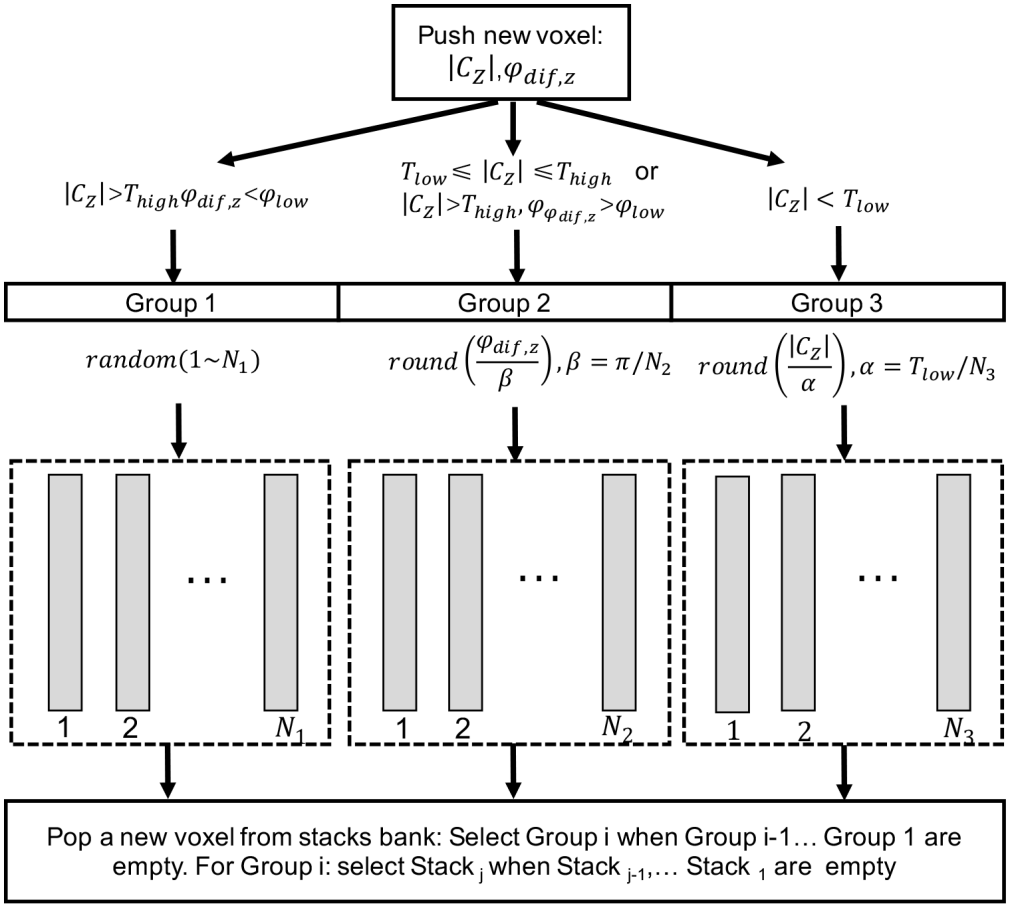

Figure 2.9: This figure demonstrates the three-tier stacks bank used to optimize the 3D-TRIPS region-growing. When pushing a new voxel into the stacks bank, the classification function is used to determine which stack to place it in based on its magnitude $|C_Z|$, and its maximum phase difference $\varphi_{dif,z}$. A new voxel is always popped up from the non-empty stack with the highest priority. See the text for more details.

Structure of three-layer grouped stacks

As mentioned previously, error propagation is the major challenge for direct phase sensitive reconstruction using region-growing. The error propagation is the problem that the error of a few voxels (mainly low SNR voxels) propagates to large region of good neighboring voxels due to the large relative weight of them. To mitigate this problem, first, M_{local} should include enough highly reliable voxels to reduce the weight of a single voxel and second, the spatial

correlation between two successive voxels during region growing should be minimized.

Based on these two requirements and supported by the Mont-Carlo simulations, a structure of three-layer grouped stacks, which we called a stacks bank, was designed to prioritize the highly-reliable voxels during region-growing. The stack is a structure from which its elements come off in the order of "last in, first out" [56, 57]. For 3D-TRIPS, the stacks bank consists of an array of stacks separated into three groups (Figure 2.9):

Group 1: The voxels in group 1 are the most reliable for background phase estimation. They have large magnitude and small maximum phase difference:

$$|C_Z| \geq T_{high} \& \varphi_{dif,z} < \varphi_{low} \tag{2.4}$$

$\varphi_{low}$is the phase threshold and is set as $\pi/6$ in this study. T_{high} is the magnitude threshold and considering the wide range of possible TI, in this study, $T_{high} = min(T_{ven}, 10 \times T_{lung})$ where T_{ven} is the threshold that covers more than 50% myocardial ventricle region and T_{lung} is the average signal intensity in the lung region.

Group 2: There are two types of voxels in Group 2. The first type are voxels with medium magnitude. The second type are the voxels with high intensity and large neighboring phase difference:

$$T_{high} \geq |C_Z| \geq T_{low} or |C_Z| \geq T_{high} \& \varphi_{dif,z} > \varphi_{low} \tag{2.5}$$

$T_{low}$is used to separate the low SNR region and is about 4 times the average signal intensity within lung region in this study. This second type are the voxels distributed in the polarity transition regions.

Group 3: Group 3 are the voxels with low SNR and are unreliable for background phase estimation:

$$|C_Z| \leq T_{low} \tag{2.6}$$

The stacks number represents its priority within each group. Group 1 includes $N_1 = 5$ stacks. Monte Carlo simulation shows that voxels with high SNR are always reliable for background

phase estimation and therefore, a new voxel of Group 1 is randomly pushed into one of the five stacks. Group 2 includes $N_2 = 36$ stacks. For a new voxel of Group 2, the stack number r_Z is determined by its maximum phase difference φ_Z and $r_Z = floor(\varphi_Z/\beta), \beta = \pi/N_2.floor(x)$. represents the maximum integer that is smaller than x. Group 3 contains $N_3 = 20$ stacks. For a new voxel V_Z of Group 3, r_Z is determined by its magnitude and is calculated as $r_Z = floor(|C_Z|/\alpha), \alpha = T_{low}/N_3$.

During region growing, the new voxel to be processed is always popped out from the non-empty stack with the highest priority and its unprocessed neighboring voxels are then pushed into the stacks bank based on the rules of each group.

The multi-layer stacks structure has several advantages. First, it computes fast with time complexity of $O(n)$. This is because the reliability evaluation of each voxel is independent of other voxels and no sorting and comparison operation is needed. Second, 3D-TRIPS uses several randomization measures to promote even distribution of region-growing. With these randomization measures, the spatial correlation between successive voxels is minimized while prioritizing the highly-reliable voxels and therefore delay the error from low SNR to high SNR voxels. To further promote the even distribution, the order of neighboring voxels was also randomized when pushing them into the stacks bank.

2.4 Validation of 3D-TRIPS

2.4.1 MRI Acquisition

15 subjects with cardiomyopathy were recruited in this study. These patients included 10 males and 5 females and their mean age is 51.2 ±15.4 years, ranging from 22 to 72 years. 3D PSIR sequence was added to the regular cardiac MR scans. A 3T wide-bore scanner (Philips Ingenia, the Netherlands) with dStream anterior and posterior coils was used. This study was approved by the local institutional review board and all subjects provided written informed consent. The scan parameters were: 2RR interval, TR/TE 5.2/2.4 ms, flip angle 25^o, spectrally selective fat suppression (SPIR), TI range: 180-320 ms (determined for each

subject with Look-Locker scout scan and the optimal TI is the time when the signal from healthy myocardial muscle is nulled), readout bandwidth: 362 Hz/pixel, reference image flip angle 5^o, FOV $350 \times 350 \times 125mm^3$, resolution: $1.9 \times 1.9 \times 10mm^3$, interpolated to $1.1 \times 1.1 \times 5mm^3$.

A pencil-beam navigator was used for respiratory motion gating (7 mm acceptance window, applied just prior to each T1 weighted acquisition). Each subject received a standard weight-based dose of 0.1 mmol/kg of gadobenate dimeglumine (MultiHance, Bracco Diagnostics, Princeton, NJ). PSIR were scanned 5-10 minutes after the injection of contrast. The 3D PSIR acquisition time ranged from 7 to 12 minutes.

To test the performance of 3D-TRIPS algorithm on a 1RR protocol without reference scan, an additional subject was scanned with both the standard 3D PSIR protocol and a 1RR protocol without reference scan (1RR interval). The parameters of both protocals were the same with previous 2RR scans except that TI was 440 ms for 2RR and 320 ms for 1RR scan (independently determined by 2RR and 1RR Look-Locker scout scan, respectively).

Both the non-phase-corrected complex images and standard PSIR images were exported from scanner after multi-coil combination in the scanner system.

2.4.2 Image analysis

Images were evaluated with both quantitative comparison and blinded review by radiologists.

Automatic analysis

S_{index} [4] was calculated to evaluate the polarity consistency between 3D TRIPS and PSIR reconstruction. S_{index} is defined as: $S_{index} = N_{correct}/N_{total}$ where $N_{correct}$ represents the number of voxels with same polarity between 3D-TRIPS and PSIR reconstruction, while N_{total} represents the total number of voxels within M_{global}. Only voxels with SNR higher than 2 [4]were involved in the calculation to remove the pure noise signals.

Blinded review

Both 3D-TRIPS images and PSIR images were reformatted to 2D images in the sagittal plane before review. Images were reviewed side-by-side by two experienced radiologists. During the review, images were separated into two groups (Group A and Group B) and the images reconstructed by the two methods were randomly assigned to Group A or Group B. For this myocardial LGE study, only partial FOV images with the size of around $200 \times 200 \times 125 mm^3$ surrounding the myocardial region were presented. Both radiologists were blinded to the reconstruction method related to each image. For each pair of 3D images, each reader ranked $(A > B, A = B, or A < B)$ based on the metrics including scar visibility, clinical acceptability, blurring and swap, which represents the region with incorrect polarity. The swap artifacts were evaluated within myocardium, blood pool, and outside of the heart.

Statistical Analysis

Binary variables were summarized as number (percentage) of subject scans preferred. Review results were analyzed using the Sign test. Comparisons were made based on the preferences of the two readers combined ($N = 30$ reads total) as well as for each reader separately ($N = 15$ subjects for each reader). For the comparison of the combined reader data, the Sign test was clustered by subject using a permutation test to account for the dependence from multiple readings of the same subject [58]. Agreement between reader ratings on whether 3D-TRIPS image quality was as good as or better than that of PSIR (3D-TRIPS $\geq$PSIR) was defined as the percentage of subjects where both readers either preferred or considered equivalent 3D-TRIPS over PSIR [ie, cases where neither reader preferred the PSIR reconstruction]. For example, if one reader rated 3D-TRIPS as preferred over PSIR and the other reader indicated no preference between the two, then that was counted as an agreement for the purpose of this calculation. All statistical calculations were conducted with STATA (version 14.1; StataCorp, College Station, Texas, US) and the statistical computing language R (version 3.1.1; R Foundation for Statistical Computing, Vienna, Austria). Throughout, two-sided tests were used, with statistical significance defined as $P < 0.05$.

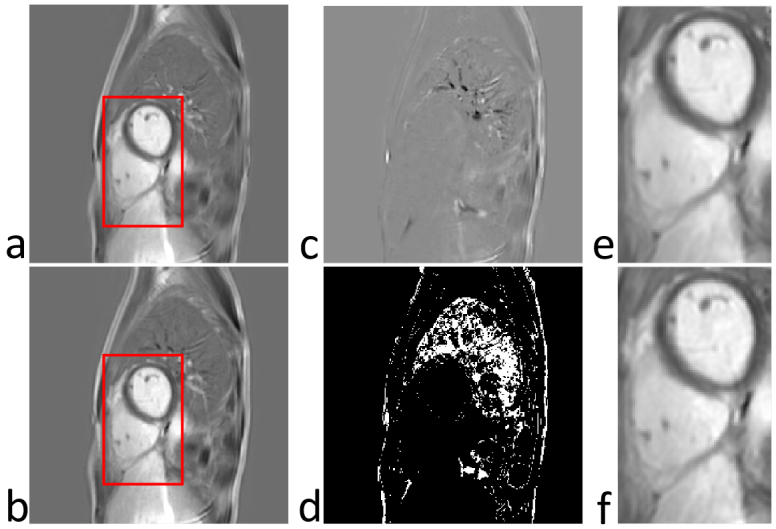

Figure 2.10: Comparison between PSIR image reconstructed by the scanner (a) and 3D-TRIPS image(b). (c) is difference map between (a) and (b). (d) representing the pixels that have different polarity between (a) and (b) which are mainly located around the low SNR region(eg. lung) and polarity transition region. (e) and (f) are enlarged areas including myocardium from (a) PSIR and (b) 3D-TRIPS (red boxes), respectively

2.4.3 Analysis results

Automatic analysis

The 3D TRIPS successfully processed the 3D images of all the 15 subjects and the computation time ranged from 4 to 6 minutes using a desktop computer. The average S_{index} of the 15 subjects is 0.950 ± 0.022, with a range of [0.900, 0.980] which demonstrates a consistent polarity between the two reconstruction methods. The images from one subject had serious motion artifacts and therefore showed relatively poor S_{index} (0.900). An example of PSIR and 3D-TRIPS images from the same slice is shown in Figure 2.10. The regions with opposite polarity mainly locate around the low SNR (eg, lung; Figure 2.10d) and polarity transition region. Small FOV myocardial images from three different subjects are shown in Figure 2.11, which demonstrate comparable image quality between the two reconstructions.

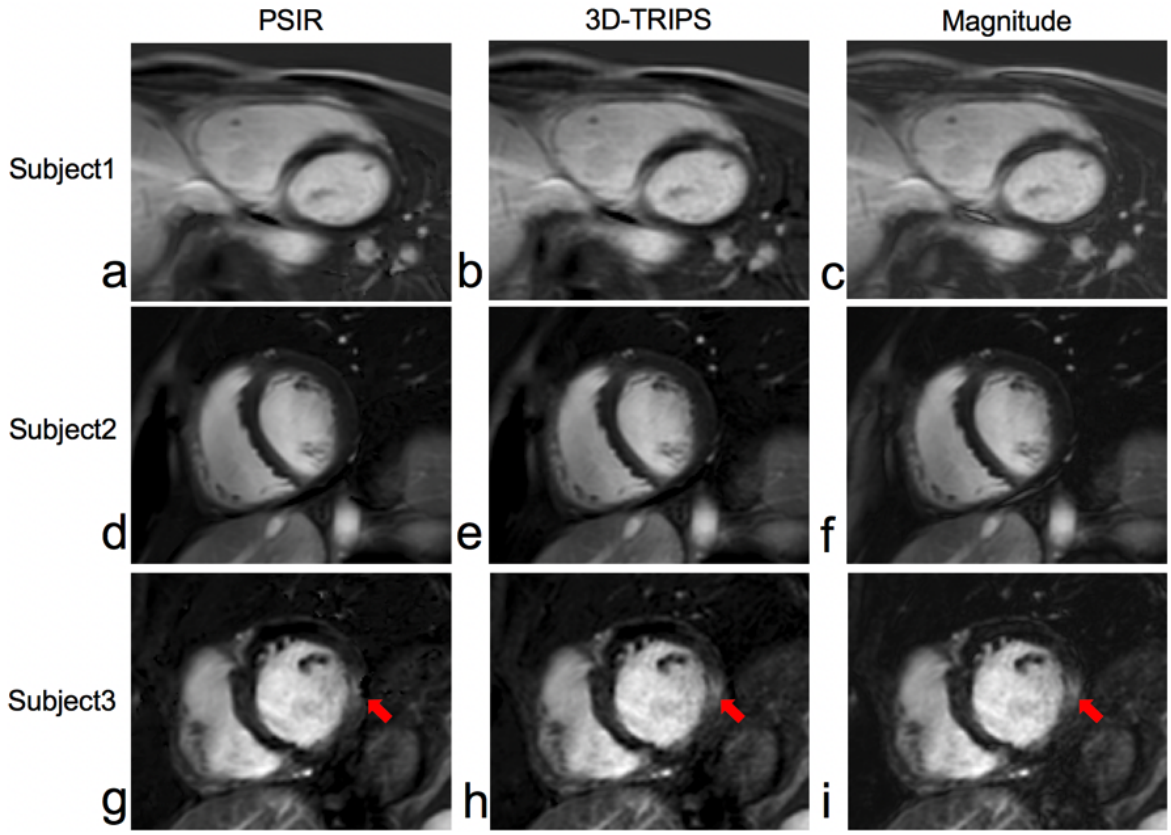

Figure 2.11: Myocardial LGE images of three patients reconstructed with PSIR (a,d,g), 3D-TRIPS (b,e,h) and magnitude (c,f,i). The images reconstructed by PSIR and 3D-TRIPS have good consistency. The third patient (g,h,i) has lateral wall LGE in the PSIR image (g), which is partially obscured by a swap artifact (red arrow). The lateral wall LGE is more prominent in the corresponding 3D-TRIPS image (h).

Further comparison between PSIR and 3D-TRIPS reveals that some artifacts(swap) in the T1 weighted images are actually transferred from the reference image (the third subject in Figure 2.11) and these artifacts are not present in 3D-TRIPS images. Figure 2.13 shows another example where artifacts in the renal cyst on the reference image are superimposed on the reconstructed PSIR image.

Comparison between 1RR 3D-TRIPS and 2RR PSIR

Figure 2.12 shows the 1RR phase sensitive image reconstructed with 3D-TRIPS and 2RR

standard PSIR. Both images show clear LGE enhancement. 3D-TRIPS image has lower SNR due to shorter interval between neighboring inversion RF pulses and sharper boundary thanks to shorter scan time.

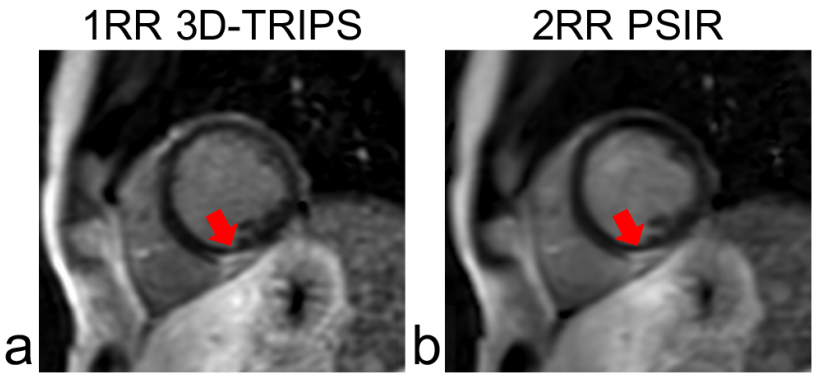

Figure 2.12: Example from one subject scanned with the standard 2RR PSIR protocol and a 1RR protocal (nominal acquisition time halved). (a) is the 3D-TRIPS reconstruction from 1RR acquisition and (b) is the PSIR reconstruction with 2RR acquisition. Note the excellent visibility of LGE at the inferior attachment site of the right ventricle (red arrow) and overall good image contrast from the 3D-TRIPS reconstruction.

Comparison between RAPID and 3D-TRIPS

RAPID is the only direct phase sensitive reconstruction method that has been validated against 2D PSIR myocardial LGE images. In this section, a 3D image with relatively poor quality was processed using RAPID reconstruction. It takes 1hour and 12 minutes for RAPID to compute the 3D data, which is much longer than 3D-TRIPS(less than 6 minutes). RAPID reconstruction has good consistency with 3D-TRIPS around the myocardial region. It, however, has swap artifacts at the abdominal region which propagates to the kidney.One slice of the subject reconstructed by both methods is shown in Figure 2.14.

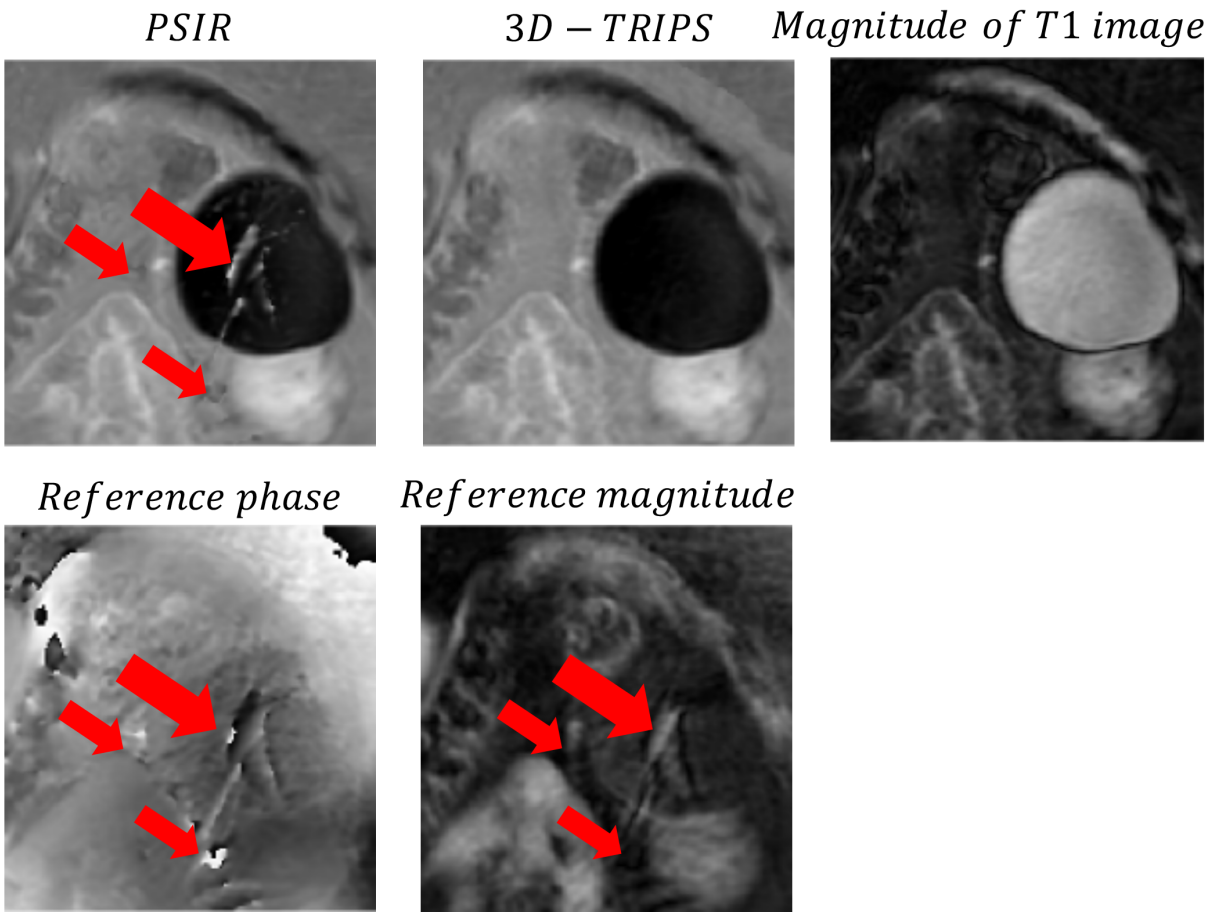

Figure 2.13: PSIR image of a renal cyst and the 3D-TRIPS image of the same slice; The artifacts in PSIR images(red arrows), transferred from the artifacts in the reference image, do not appear in 3D-TRIPS image.

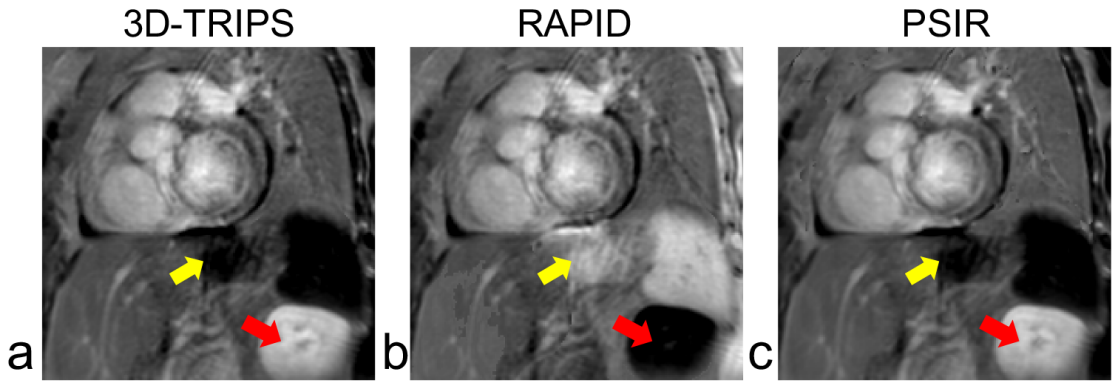

Figure 2.14: Phase sensitive images reconstructed with 3D-TRIPS(a), RAPID(b), and PSIR(c). The image quality of this subject is relatively poor with low SNR in the abdominal region. RAPID and 3D-TRIPS images are largely consistent with PSIR in the myocardial region. In the RAPID image, however, the polarity is incorrectly calculated in the low SNR region (yellow arrow), which propagates to the kidney (red arrow).

Blinded Review results

First, the review results from two readers were combined together and therefore had 30 subjects (Table 2.1). 3D-TRIPS images are preferred over PSIR with less swap artifacts both around the myocardial region (53%vs.3%, p=0.001) and outside the heart (70%vs.17%, $p = 0.010$). 3D-TRIPS images also show less blurring (57%vs.7%, $p = 0.007$) artifacts and have a higher clinical acceptability rating. In addition, reviewers found three cases with scar in 3D-TRIPS images and found no cases with scar in PSIR images (10%vs.0%, $p = 0.25$).

The review results of each reviewer were then analyzed separately (Table 2.2). Both reviewers found that 3D-TRIPS images were significantly better with less blurring (p=0.031 and p=0.022, respectively) relative to PSIR. Reviewer 1 found 3D-TRIPS images had less swap both in the myocardial region (p<0.001) and outside the heart (p<0.001), while reader 2 tended to numerically prefer 3D TRIPS over PSIR related to these metrics (p=0.38 and p=0.55, respectively). Both reviewers agreed in $73-100\%$ of the 15 subjects that 3D-TRIPS images had equal or better quality than PSIR based on all metrics (Table 2.2, last column).

Table 2.1: Preferred image across image quality metrics using the combined review by two readers.

	$PreferedImage$		
Metric	PSIR	3D-TRIPS	*P value*
Scar visibility	0(0%)	3(10%)	0.25
Less Swaps			
Myocardial swaps	1(3%)	16(53%)	0.010
Blood pool swaps	0(0%)	0(0%)	-
Swaps outside the heart	5(17%)	21(70%)	0.007
Blurring	2(7%)	17(57%)	0.064
Clinical acceptability	0(0%)	5(17%)	0.001

Table 2.2: Preferred image by each reader and their agreement.

	Prefered Image by Reader 1			Prefered Image by Reader 2			Agreement
Metric	PSIR	3D-TRIPS	P value	PSIR	3D-TRIPS	P value	3D-TRIPS $\geq$ PSIR
Scar visibility	0 (0%)	0 (0%)	-	0 (0%)	3 (20%)	0.25	15 (100%)
Less Swaps							
Myocardial swaps	0 (0%)	12 (80%)	<0.001	1 (7%)	4 (27%)	0.38	14 (93%)
Blood pool swaps	0 (0%)	0 (0%)	-	0 (0%)	0 (0%)	-	15 (100%)
Swaps outside the heart	1 (7%)	14 (93%)	<0.001	4 (27%)	7 (46%)	0.55	11 (73%)
Blurring	0 (0%)	6 (40%)	0.031	2 (13%)	11 (74%)	0.022	13 (87%)
Clinical acceptability	0 (0%)	2 (13%)	0.50	0 (0%)	3 (20%)	0.25	15 (100%)

2.5 Discussion

In this section, 3D-TRIPS with a three-layer stacks bank was introduced to directly reconstruct the 3D myocardial phase sensitive images in a fast and reliable fashion. 3D-TRIPS was validated on 15 subjects both subjectively and objectively, 3D-TRIPS images showed good image quality and consistency compared with PSIR images.

2.5.1 Advantages of 3D-TRIPS

Advantages over PSIR

Compared with 2D MRI images, 3D images have higher SNR and therefore can support higher resolution. 3D isotropic high resolution LGE images allow for a better characterization of LGE subjects. 3D LGE imaging, however, is restricted with the conventional PSIR due to the prolonged scan time for fully sampled reference scan. The prolonged scan time may introduce more T1 variation and motion artifacts that compromise the image quality of the entire scan. MRI acceleration acquisition and reconstruction methods, such as parallel imaging [17], compressed sensing or combination of them [59] can significantly improve the scan efficiency. These methods, however, have the problems such as lower SNR [60], missing fine structure due to "global ring" and blurring artifacts [61] and extra effort for reconstruction parameters optimization [62]. 3D-TRIPS, on the contrary, halves the scan time of PSIR without compromising image quality.

3D-TRIPS separate voxels into three groups with different priority and within each group, the stacks are also ranked. Despite of this group separation, the stacks of 3D-TRIPS are largely continuous. For example, voxels in the first stack in Group 2 can also be categorized into Group 1 without compromising the accuracy. Besides, compared with RAPID, which simply emphasizes on prioritizing the good voxels, 3D-TRIPS pays equal attention to delaying the "bad voxels". These features make 3D-TRIPS not sensitive to the selection of parameters, like the thresholds between groups.

In this section, both reviewers preferred 3D-TRIPS images over PSIR images on several

metrics. In addition, PSIR images showed more artifacts not existing in the 3D-TRIPS images and the major source of these artifacts is the motion between the two acquisitions.

Advantages over other direct phase sensitive reconstruction method

One major challenge with conventional direct phase sensitive reconstruction is the error propagation which is caused by 1) the small number of low quality voxels covered by M_{local} and 2) high spatial correlation between successive voxels during region-growing. 3D-TRIPS uses a three layer stacks bank to optimize the region-growing track based on intensity instead of phase. Supported by the Monte Carlo simulation, signal intensity and maximum phase difference are used to determine the priority of voxels and therefore improve the overall quality of the voxels covered by M_{local}. Compared with RAPID method, 3D-TRIPS has several advantages:

First, 3D-TRIPS relies on SNR or signal intensity to optimize the region growing track and therefore minimize the influence of the low SNR voxels to high SNR voxels.

Second, randomization of growing track was emphasized to further reduce the geometric correlation between two successive voxels during region-growing through: 1) randomization of the order of neighboring voxels when pushing them into the stacks and 2) using a large number of stacks in each group. These randomization measures promote even distribution of region growing tracks and (in an unlikely event) if an error happens on a low SNR voxel, its influence will be offset by the neighboring good voxels with correct background phases.

Third, RAPID needs to sort the phase to determine the priority of region growing, the time complexity of major sorting algorithm is$O(n2)orO(nlog(n))$where n is determined by the number of voxels. RAPID needs longer time (typically over one hour) to process 3D images and is only eligible for 2D images. On the other hand, 3D-TRIPS does not need the sorting operation and can process 3D image calculation within a much shorter time (typically a few minutes). With 3D images, 3D-TRIPS allows for a larger number of reference voxels to be covered by M_{local}. Furthermore, the better connection condition of high SNR voxels in 3D images can further reduce the error propagation.

2.5.2 Comparison with phase unwrapping

The phase wrapping problem can be expressed in the following equation: $\varphi_{wrapped} = \varphi_{unwrapped} - 2k\pi, k = 0, \pm1, \pm2....., \varphi_{wrapped} \in (-\pi, \pi]$, This equation shows that an unwrapped phase will be wrapped in the phase image(Figure 2.15). To recover the continuity of phase between neighboring pixels, phase unwrapping is needed. When doing phase unwrapping, a reference voxel will be used as the starting point and region-growing is usually used to gradually calculate the unwrapped phase of each voxel. During region-growing, if the apparent phase difference($\varphi_{dif} = \varphi_1 - \varphi_{ref}$ or $\varphi_{dif} = angle(S_1) - angle(S_{ref})$,where $S_1 and S_{ref}$represent the complex MRI signal) between two neighboring voxels is too large (like $> 3\pi/2$), 2π will be added or removed from the phase of the target voxel.

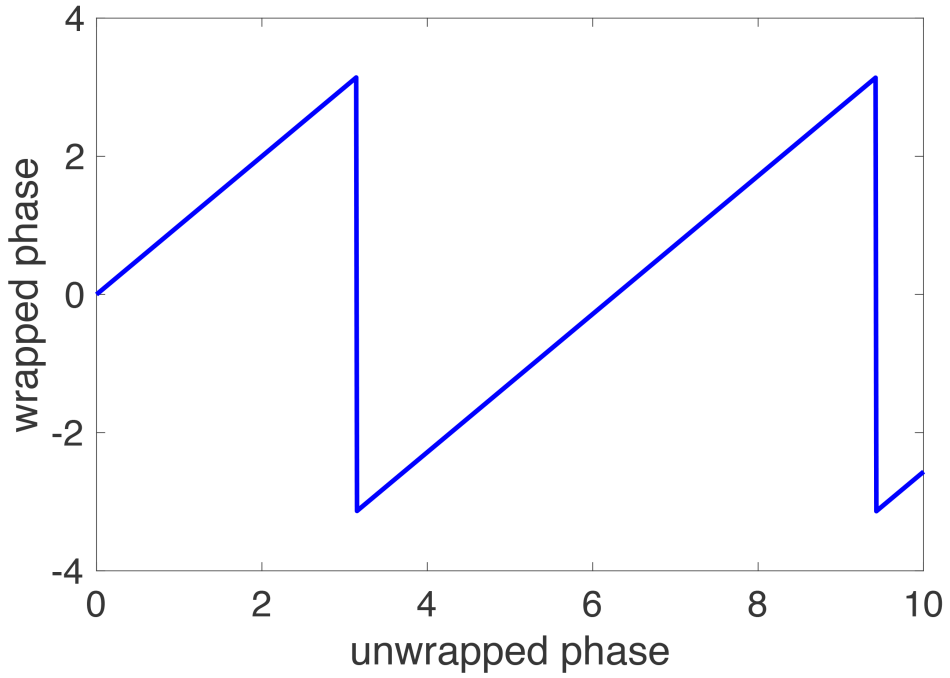

Figure 2.15: the continuous phase is wrapped to the range of $(-\pi, \pi]$, and wrapping happens when the apparent phase is $2k\pi - \pi, k = 0, \pm1, \pm2.....$

In this study(3D-TRIPS), to recover the true phase, the phase difference is calculated as: $\varphi_{dif} = angle(S_1 \times conjugate(S_{ref}))$. Therefore, the phase difference and threshold

selection will only be determined by the angle instead of apparent phase difference between two complex vectors. 3D-TRIPS does not have phase wrapping problems.

2.5.3 Selection of seed

For 3D-TRIPS, the seed voxel of region-growing is randomly selected from a high-intensity region within the blood pool. With the three-layer stacks, the region-growing prioritize the growing within 1) high-SNR region 2) region with same polarity. This means that although the region-growing of 3D-TRIPS is optimized voxel by voxel, it also grows in the unit of block: block of same polarity or same intensity level. For myocardial LGE images, the high-SNR blood pool region is surrounded by the low-SNR myocardium region. Therefore, whichever the seed voxel is, the region-growing will first complete the high-SNR blood pool region, which are extremely reliable. From another point of view, for myocardial LGE imaging, the seed is actually the whole high SNR blood-pool region instead of a single voxel and therefore the selection of seed voxel will not influence the result.

Other advantages to start from the blood pool is that 1) the myocardial region is the region of interest 2) the structure of left ventricle blood pool is convex structure and therefore further reduce the risk of error propagation from low SNR voxels to high SNR region. For full automation of 3D-TRIPS, the seed selection method can either be that used in RAPID(small continuous region with small gradient)[4] or by using the average of a small high SNR region(3x3x3, for example) near the central of blood pool of left ventricle.

2.5.4 Problems with 3D-TRIPS methods

3D-TRIPS has several problems:

First, 3D-TRIPS may fail in large continuous regions with low SNR due to lack of high-quality voxels covered by M_{local}. A possible solution is to start the region-growing simultaneously from several seed points [54] with prior knowledge of polarity distribution [63].

Second, like other direct phase sensitive reconstruction methods, 3D-TRIPS cannot recover the background phase induced by the chemical shift, particularly the fat-water chemical

shift. Previous research showed that an in-phase TE can reduce the chemical shift phase from fat. In this study, an in-phase TE (2.4 ms) was used. In addition, fat suppression RF pulse was applied to further suppress the fat signal. Even there is still residual fat signal, a voxel with large phase difference introduced by fat will be placed into Group 2 of 3D-TRIPS to further delay its influence to good voxels.

Finally, 3D-TRIPS was developed based on the hypothesis that the background phase map is spatially smooth. This hypothesis, however, is not valid around the tissue/air transition areas or tissues boundaries. The influence of small regions with sub-optimal background phase on the voxels in 'good' region can be offset by the low pass filter in the final step of 3D-TRIPS. Furthermore, the non-smooth background phase in the reference images may cause artifacts in its neighboring region of phase sensitive images by the motion between two acquisitions of PSIR.

2.5.5 Future work

3D-TRIPS is not restricted to myocardial LGE imaging. It can also be applied on other phase sensitive reconstruction applications such as SNAP or Dixon water-fat quantification.

2.6 Summary

By using the three-layer stacks bank, 3D-TRIPS can directly reconstruct 3D phase sensitive myocardial LGE images with good quality. The scan time of 3D-TRIPS acquisition is only half of conventional PSIR. This method has the potential to make 3D myocardial phase sensitive imaging more feasible for clinical application.

Chapter 3

SPECIFIC AIM 2: IDENTIFY THE COMPONENTS OF INTEREST(LUMEN) WITH OPTIMIZED PHASE SENSITIVE MRI

3.1 Background

Compared with other MRI images, phase sensitive images have two contrasts: intensity contrast and polarity contrast. Unlike intensity contrast, polarity contrast is a binary contrast, which is convenient for segmentation and less sensitive to artifacts, and therefore is advantageous in the detection of tissue boundary. In this section, lumen detection assisted by the polarity map of SNAP will be used as an example to evaluate the accuracy of tissue contour identified by the polarity contrast of phase sensitive images.

Currently, luminal stenosis is the major clinical metric to evaluate the risk of atherosclerosis plaques. Surgery is usually suggested to symptomatic patients with stenosis degree higher than 70% [64].

CE-MRA relies on the intravenously injected contrast agents to shorten the T1 of blood and thereby can produce reliable lumen contrast[65]. Previous studies showed that CE-MRA has a good sensitivity and specificity for stenosis measurement in the carotid artery [66].The injected contrast agents, however, may induce allergic reactions and nephrogenic systemic fibrosis which are life-threatening to the patients with chronic kidney disease[65].

Non-contrast MRA, like TOF[66] and phase contrast MRA[66, 67] are alternative non-invasive MRI tools for luminal stenosis measurement without the risk of contrast agents. Among these methods, TOF is most commonly used because of its relatively short acquisition time[68]. During TOF acquisition, the static tissues are saturated by the repeated RF pulse while the lumen is refilled with fresh blood. Therefore, TOF heavily relies on the blood

refreshment to produce lumen contrast and is sensitive to flow artifacts[69]. Previous study shows that TOF may overestimate the luminal stenosis[70].

SNAP can simultaneously detect IPH and luminal stenosis with the recovered polarity map. Currently, only intensity contrast of SNAP MRA is used for stenosis measurement and the polarity information is not fully used.

In this section, aided by the objective gradient map or polarity map, the lumen size and stenosis measurements were compared between SNAP and 3D-TOF, using CE-MRA as the reference standard.

3.2 Sequence validation

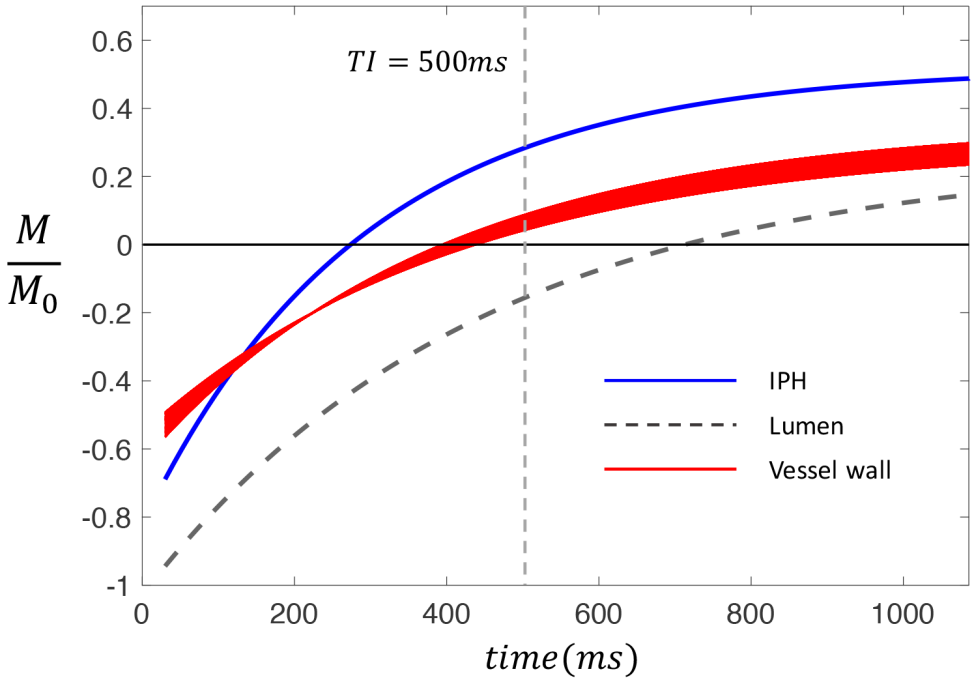

Figure 3.1: Simulation of release trajectory of IPH(blue line) , lumen (grey dot) and vessel wall(red line) during SNAP scan. This simulation verifies that only lumen has negative polarity in SNAP MRA.

SNAP is optimized that the polarity of IPH and lumen are positive and negative respectively while the signal of vessel wall is nulled. To identify the lumen using the negative polarity of SNAP MRA, we need to guarantee that the polarity of vessel wall is positive. This hypothesis was verified through a simulation. In this simulation, the SNAP parameters were as follows: TR: 10ms, TFE factors: 98, $FA_{T1} : 11^o; FA_{ref} : 5^o$. T1 of IPH is 500ms and T1 of blood is 1550ms. Also in this simulation a large range of T1 was used for vessel wall(965-1265ms). As can be seen in Figure 3.1, this simulation verifies that only lumen has negative polarity in SNAP MRA.

3.3 Experiment Design

3.3.1 Subjects

Eleven subjects (72.1±8.6 years; 9 males) were selected from a prospective cohort study on the natural history of carotid atherosclerosis. Each subject has $16 - 79\%$ asymptomatic carotid stenosis, in at least one carotid artery identified with duplex ultrasound. All the eleven patients were scanned with SNAP, 3D-TOF and CE-MRA. 15 carotid arteries from these eleven patients had$> 0\%$ luminal stenosis identified on CE-MRA images according to the NASCAET[41] criteria and were included in this study. Among those eleven patients, nine were male and two were female. This study was approved by the local institutional review board and written informed consent were obtained from all subjects before the scan.

3.3.2 MRI imaging protocol

Patients were scanned on a 3T whole body scanner (Philips Achieva, R3.2.1, Netherlands). A custom-designed eight-channel phase-array surface coil (Chengguan Medical technologies, Shanghai, China) was used for SNAP and 3D-TOF scan. CE-MRA was scanned with the embedded body coil. SNAP parameters were optimized [8]to maximize the IPH/vessel wall and vessel wall/lumen contrast. The optimized parameters were as follows: TR/TE: 9.8/4.72ms, TI: 500ms, $FA : 11^o$, FOV: 160(Foot-head (FH) direction)×160(Right-Left (RL)

direction)×32(Anterior-Posterior(AP) direction)mm^3, acquisition resolution: $0.8 \times 0.8 \times 0.8mm^3$and was interpolated to $0.4 \times 0.4 \times 0.4mm^3$.

3D-TOF parameters were: TR/TE: 20/4.9ms, FA: 20^o, FOV: 160(FH)×160(RL)×48(AP)mm^3, resolution was $0.6 \times 0.6 \times 2mm^3$ and was interpolated to $0.3 \times 0.3 \times 2mm^3$.

For CE-MRA, 0.1 mmol/kg of Gd DTPA (Magnevist, Bayer Healthcare, Wayne, NJ) contrast agent was injected to each patient at a rate of 2ml/second and was followed by the same volume of saline flush. The scan parameters of CE-MRA were: TR/TE: 5.5/1.7ms, FOV: 350 (FH) ×350(RL) ×64(AP) mm^3, FA: 30^o, resolution: $0.8 \times 0.8 \times 0.8mm^3$ interpolated to $0.4 \times 0.4 \times 0.4mm^3$.

To determine distribution of plaque burden and differentiate segments with (diseased) and without plaque(healthy), 3D MSDE prepared Rapid Gradient Echo (3D-MERGE) (51), was also added to the scanned sequence. Its parameters were: TR/TE: 10/4.8ms, FA: 6^o, FOV: 250(FH)×250(RL)×42(AP)mm^3, resolution: $0.8 \times 0.8 \times 0.8mm^3$, interpolated to $0.4 \times 0.4 \times 0.4mm^3$.

3.3.3 Image review

Coronally acquired SNAP, CE-MRA and 3D-MERGE images were first reformatted to transverse slices with the slice thickness of 2mm. Slices of four sequences were matched using bifurcation as reference. 21 slices centered at the bifurcation of common carotid artery (1 slice at the bifurcation, 10 consecutive slices proximal to the bifurcation, 10 consecutive slices distal to the bifurcation) were included in image analysis. Slices which were not covered by any of the three sequences (SNAP, CE-MRA and 3D-TOF) were excluded from the study.

A custom-designed image analysis software package (CASCADE 2.0, University of Washington, Seattle, WA)[71]was used to review images and draw the lumen boundary. TOF, SNAP and CE-MRA images were read independently in three separate reading sessions. For each reading session, slices of each sequence were pooled together and presented in a random order to the reader. In this way, the lumen boundary of each slice was determined independently without referring the neighboring slices or slices of other sequences.

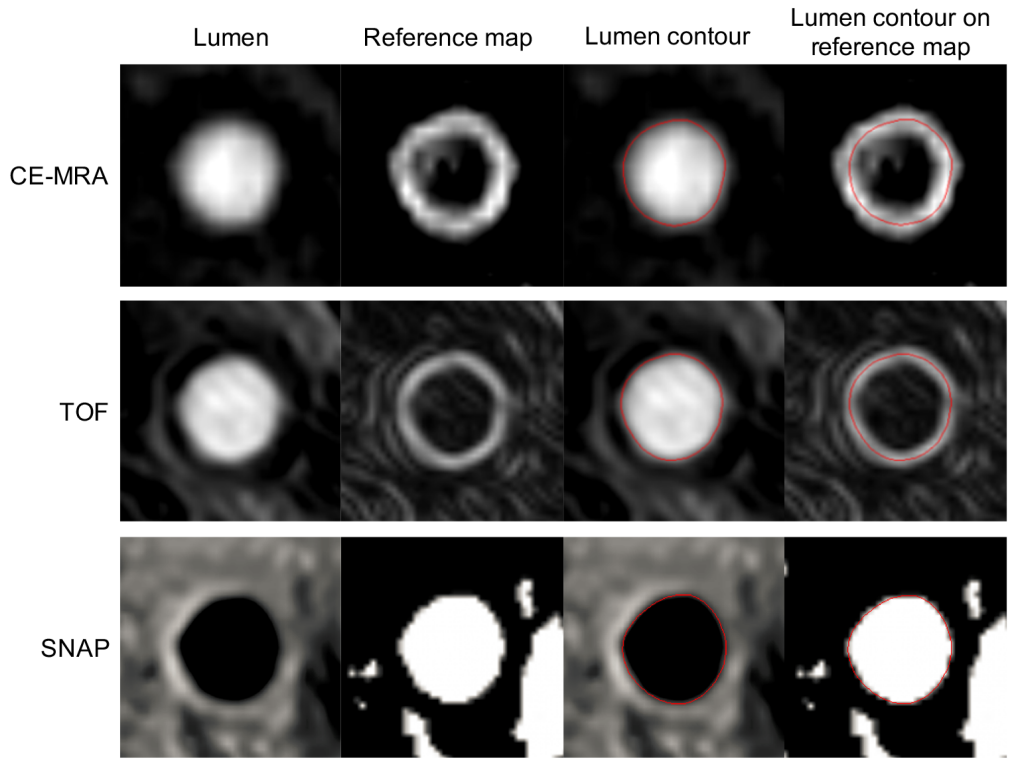

Figure 3.2: Comparing CE-MRA, TOF and SNAP in delineating carotid lumen. The first two columns are original images and corresponding reference maps. Reference map in CE-MRA and TOF is a gradient map generated with the Sobel filter. Reference map in SNAP is a polarity map that marks regions with negative signal. The last two columns show lumen boundaries defined based on reference maps. Lumen boundary is defined along the highest gradient in CE-MRA and TOF and around the region with negative polarity in SNAP

The lumen boundary was drawn semi-automatically for all three sequences. A gradient map was generated with Sobel operator[72, 73] for TOF and CE-MRA and the lumen boundary was drawn along the contour with the highest gradient (Figure 3.2). For SNAP, the negative polarity map was used to identify lumen boundary(Figure 3.2).

A reader with seven years of multi-contrast carotid MRI review experience read the reformatted 3D MERGE images and classified the slices into diseased and healthy groups based on the presence of distinct focal wall thickening ($\geq 1.5mm$). After obtaining the measured lumen size of all matched slices, the percent luminal stenosis was calculated for

each artery as 100%x(minimum lumen area / reference lumen area). To mimic the NASCET criteria, if the stenosis was in internal carotid artery, the reference was chosen as a distal normal slice beyond carotid bulb or as a proximal normal slice if the stenosis was in common carotid artery.

3.3.4 Statistical Analysis

Overall agreement of lumen size and luminal stenosis between SNAP, TOF, and CE-MRA was evaluated using the intraclass correlation coefficient (ICC). Bias and limits of agreement were evaluated using the Bland-Altman plot (difference versus mean between two sequences). Bland-Altman limits of agreement (mean difference ±1.96*standard deviation of differences) was also calculated.

Confidence intervals (CIs) were calculated using bootstrapping. Slices were randomly resampled in the unit of subject which means that slices of the same subject were always resampled together.

Bias in lumen area and percent luminal stenosis relative to CE-MRA was tested against 0 using a permutation test based on the paired t-test. Similar to the bootstrapping test, permutation test was also resampled in the unit of subject. Statistical analysis were performed with Matlab (R2014b, Mathworks, Natrick, MA).

3.4 Results

Of the 315 slices, eighteen slices were outside the foot-to-head coverage of TOF and eight slices were outside the FOV of SNAP images. Therefore, a total of 289 matched slices were reviewed with all three sequences. Among them, 137 (47%) had plaque and were categorized as diseased slices.

Agreement of lumen size measurement

$TOF vs. CE-MRA$

As shown in Table 3.1 and Figure 3.3a, the ICC between TOF and CE-MRA across all slices

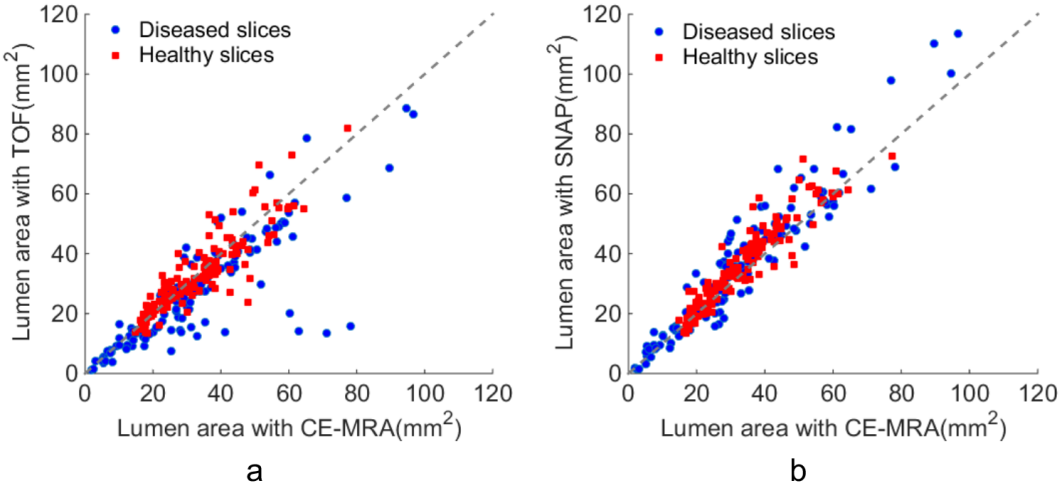

Figure 3.3: Scatter plots on the agreement of TOF and SNAP with CE-MRA in measuring carotid lumen area. A total of 289 matched MR slices were included, 137 (47%) of which had plaque as detected in black-blood vessel wall MRI (blue dots). ICC was 0.83 (95% CI: 0.70, 0.93) for TOF (a) and 0.93 (95% CI: 0.89, 0.96) for SNAP (b).

was 0.83 (95% CI: 0.70, 0.93). As to each sub-group, the ICC appeared to be lower in the sub-group with plaque (ICC: 0.80 [95% CI: 0.60, 0.93]) and higher in the healthy sub-group (ICC: 0.89 [95% CI: 0.83, 0.93]). The lumen size measured on TOF images was smaller on average than that measured on CE-MRA images with a negative bias of -2.6mm^2 (P<0.001; Figure 3.4a). This negative bias was majorly introduced by the diseased slices (-5.1 mm^2; P<0.001) there was no apparent bias in the healthy sub-group (-0.4 mm^2, P=0.45).

$SNAP vs. CE-MRA$

The overall agreement between SNAP and CE-MRA (ICC: 0.93 95% CI: 0.89, 0.96) (Table 3.2 and Figure 3.3b) was higher than that of TOF (P =0.03). The agreement was consistent in slices without (ICC: 0.91 [95% CI: 0.86, 0.96]) and with plaques (ICC: 0.93 [95% CI: 0.90, 0.96]).

The lumen area measured on SNAP has a positive bias (+2.9 mm^2; P <0.001; Figure 3.4) relative to the CE-MRA images. This positive bias was consistent with the healthy (2.8

Table 3.1: Lumen size measurements on TOF and CE-MRA

	Number of Slices	TOF(mm^2)	CE-MRA(mm^2)	Difference(mm^2)	P value	ICC	95%CI
All slices	289	30.3±15.0	32.9±15.8	-2.6±8.7	<0.001	0.83	0.70, 0.93
Diseased	137	27.6±17.1	32.7±19.0	-5.1±10.6	<0.001	0.80	0.60, 0.93
Healthy	152	32.7±12.5	33.1±12.3	-0.4±5.7	0.45	0.89	0.83, 0.93

Table 3.2: Lumen size measurements on SNAP and CE-MRA

	Number of Slices	SNAP(mm^2)	CE-MRA(mm^2)	Difference(mm^2)	P value	ICC	95%CI
All slices	289	35.8±18.0	32.9±15.8	2.9±5.9	<0.001	0.93	0.89, 0.96
Diseased	137	35.7±21.8	32.7±19.0	3.1±6.9	<0.001	0.93	0.90, 0.96
Healthy	152	35.8±13.9	33.1±12.3	2.8±4.9	<0.001	0.91	0.86, 0.96

mm^2; P <0.001) and diseased slices (3.1 mm^2; P <0.001)

Agreement of stenosis measurement

Table 3.3: Percent luminal stenosis measurements

	Stenosis	Bias compared to CE-MRA	P value	ICC (95% CI)
CE-MRA	$52 \pm 20\%$	NA	NA	NA
TOF	$56 \pm 19\%$	$4.0 \pm 9\%$	0.08	0.88(0.67, 0.96)
SNAP	$54 \pm 22\%$	$1.5 \pm 7\%$	0.46	0.94(0.82, 0.98)

Percent luminal stenosis based on lumen area shows a high agreement with CE-MRA for

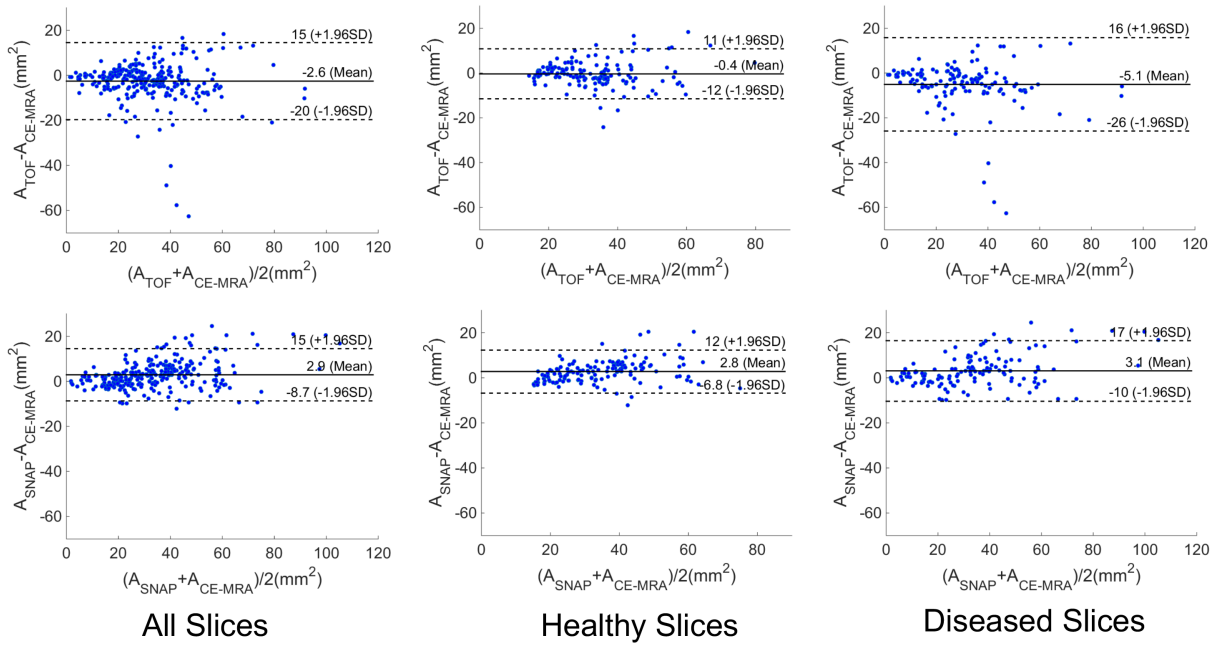

Figure 3.4: Bland-Altman on the bias of lumen size measurements between TOF and CE-MRA and between SNAP and CE-MRA. Matched slices are classified into healthy and diseased sub-group. Mean differences and 95% limits of agreements are shown.

both TOF (ICC: 0.88; 95% CI: 0.67, 0.96) and SNAP (ICC: 0.94; 95% CI: 0.82, 0.98) (Table 3.3). The mean differences in percent luminal stenosis compared with CE-MRA were 4.0% (P=0.08) for TOF and 1.5% (P=0.46) for SNAP.

3.5 Discussion

In this study, the accuracy of lumen size identified by the negative polarity of SNAP MRA was compared with 3D TOF using CE-MRA as the reference. This study showed that lumen determined by the negative polarity of SNAP has higher agreement with CE-MRA than 3D TOF. Besides, both the lumen size and bias show good consistency in the healthy and diseased sub-groups. In comparison, TOF underestimates the luminal stenosis and showed larger bias and lower agreement because of flow artifacts in the diseased sub-group. Our study demonstrates the potential of SNAP as an alternative to TOF for stenosis measure-

ment and more importantly the potential of using polarity of phase sensitive image to identify the risk factors.

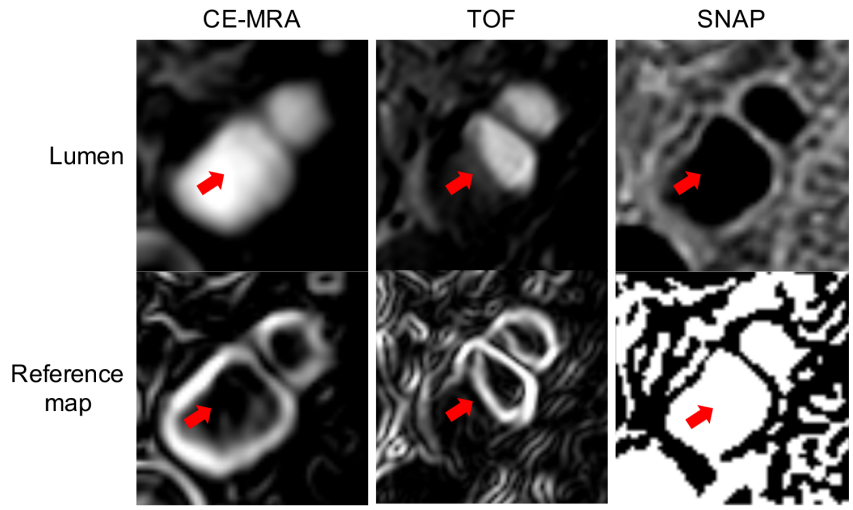

Figure 3.5: A representative slice with flow artifacts on TOF. Top row shows original images of CE-MRA, TOF, and SNAP. Bottom row shows corresponding reference maps. Red arrows indicate a region with turbulent flow that shows as flow artifacts on TOF but not on SNAP.

Advantage of SNAP with turbulent flow artifacts

CE-MRA is not sensitive to flow artifacts because its lumen/vessel wall contrast relies on the shortened T1 induced by the contrast agent.

For 3D-TOF, the lumen contrast depends on the TR of RF pulses and refreshment rate of blood. Due to the short TR (25-50ms)[68] , slow or turbulent flow will experience more RF pulses and therefore has hypointense signal relative to regular flow. Our study showed that TOF tends to overestimate the stenosis and has larger negative bias relative to CE-MRA at the region vulnerable to turbulent flow. This finding is consistent with previous research [74].

Inversion recovery RF pulses are used with SNAP to produce lumen contrast which has several advantages over TOF on flow artifacts. First, its lumen contrast relies majorly on

the T1 difference instead of flow refreshment. Second, the long interval between inversion pulses (2s) allows the full refreshment of blood within a large FOV. In this study, the FOV of SNAP is much larger in the coronal dimension than 3D-TOF (160mm vs. 46mm). This feature is important when stenosis exists distantly from the bifurcation of carotid artery. Third, SNAP sequence is optimized that the polarity of lumen is negative while the polarity of vessel wall and IPH is positive. The recovered polarity doubles the dynamic range of contrast [8]. Besides, the lumen contour identified by the binary polarity map is less sensitive to flow artifacts. A region with negative polarity can be reliably identified as lumen even with a small intensity contrast (Figure 3.5).

The positive bias of SNAP vs CE-MRA

To reduce the individual bias of readers, maximum gradient contour was used to determine the lumen boundary in TOF and CE-MRA images in this study. This contour is actually within the lumen and the area within this contour is smaller than the actual lumen size. For SNAP, the negative polarity can well approximate the true lumen size. Therefore, lumen size measured on SNAP has a consistent positive bias relative to CE-MRA and the bias was mitigated in stenosis measurement.

MIP vs. lumen size

Currently, stenosis measured on MIP images is clinically used to evaluate the risk of atherosclerosis plaque. MIP images are similar to 2D DSA images, which are clinical gold standard. Fine structure and low-intensity region around stenosis, however, may be lost [75] in the MIP images and luminal stenosis may be underestimated when the shape of lumen is asymmetric [66]. 3D MRA tools, like CE-MRA, 3D TOF and SNAP allow the luminal stenosis to be quantified more accurately[76].

Semi-automatic measurement of lumen stenosis

Assisted by the polarity map, SNAP showed a good agreement on lumen size and stenosis

measurement with CE-MRA. This study shows the potential of automatic lumen contour detection with SNAP MRA which can solve the problems like model training and magnitude or gradient threshold optimization with major auto-segmentation methods [63, 76, 77].

Study limitation

This study has several limitations:

First, CE-MRA instead of DSA was used as the reference. DSA is the clinical gold standard for luminal stenosis measurement. DSA can only quantify one-dimensional luminal stenosis while in this study the luminal stenosis was calculated using 2D lumen area. In addition, previous study verified that CE-MRA has good sensitivity and specificity on stenosis measurement using rotational angiography as reference[66, 67].

Second, only 15 arteries were included. Nonetheless, analyses were designed to be performed at the slice level, considering that complex flow conditions may be present locally and cause subtle differences in lumen area measurements.

3.6 Summary

In this study, lumen contour identified by the negative polarity of SNAP MRA was evaluated against CE-MRA. This study shows that SNAP can serve as an alternative non-contrast MRA to TOF. This study also shows the advantages of SNAP MRA on automatic lumen segmentation and quantification assisted by the binary polarity map and the binary polarity map is less sensitive to flow artifacts relative to gradient map. Furthermore, this study shows that the polarity map of optimized phase sensitive images can be used to detect and quantify other tissues of interest.

Chapter 4

SPECIFIC AIM 3: IMPROVE SNAP FOR CALCIFIED NODULES DETECTION AND ARTERY/VEIN SEPARATION ASSISTED BY THE BINARY POLARITY MAP

4.1 Study goal

For SNAP, only the phase part of the reference image is used to help remove the background phase. To achieve high SNR, the magnitude part (M_2)of the reference image is optimized to be a PD weighted image. Currently, M_2 is not used which makes SNAP time inefficient. Besides, SNAP cannot separate the arteries from veins which may be the challenge for the studies that focus only on the pathological characteristics of arteries or veins. This section includes two subsections. In this first section, M_2 will be used to identify the calcified nodules near the thin fibrous cap supported by the findings that lumen of SNAP MRA can be reliably identified by the polarity map. In the second section of this study, arterial and veinous lumen were separated on SNAP MRA assisted by an artificaly constructed binary mask.

4.2 Calcification detection with the reference image of SNAP

Calcification [13, 26], especially calcified nodules near the fibrous cap, is an important predictor for high-risk atherosclerosis plaques. Since calcification has hypointense signal in the PD weighted image[88], M_2 can be used for calcified nodules detection. To identify calcified nodules near the thin fibrous cap, both black/grey and bright blood MRA are needed. And reliable lumen boundary is unavailable with M_2 images. In this study, the black/grey blood PD image with M_2 are produced through both transferring lumen of SNAP MRA to M_2 and applying the blood suppression preparation pulses with SNAP.

4.2.1 Black/grey-blood PD weighted MRA on the reference image of SNAP

To identify the location of calcified nodule, especially those near the thin fibrous cap, a post-processing tool is developed to produce black blood/grey blood PD weighted image(SNAP2) using M_2.

In Chapter 3, it's validated that the lumen can be reliably identified by the negative polarity of SNAP MRA. In this section, we try to transfer the lumen contour from the SNAP MRA to M_2.

Step1: Remove the positive region from SNAP MRA and keep only the negative region S_-.

Step2: Use a median filter to remove the noise voxels from S_- and keep only the lumen region through the selection of large connected regions with high SNR.

Step3: For each lumen region, a weight map $W_- \in [0, 1]$ is produced based on the intensity distribution within the lumen of SNAP MRA. W_- is then multiplied with M_2 to produce SNAP2 images(M_{SNAP2}). W_- is calculated as:

$$I_{d,j} = max(1 - \frac{I_i - I_{min}}{I_{max} - I_{min}} \times a, 0) \tag{4.1}$$

In this equation (4.1) ,$I_{d,j} \in [0, 1]$ and represents the weight of a voxel in W_- map. I_i is its intensity in the SNAP MRA. I_{min} and I_{max} are the minimum and maximum intensity within the lumen. a is a coefficient larger than 1 to limit the weight of voxel with extraordinarily intensity.

The advantage of using weight map instead of direct lumen segmentation is that the original lumen boundary of SNAP MRA can be kept with minimum artificial intervention.

Step4: If grey blood MRA M_{grey} is needed, it can be calculated as: $M_{grey} = (1 - b)M_2 + bM_{SNAP2}$ Where b is a small coefficient$\in$[0, 1].

Results

This method was successfully applied on both intracranial artery and carotid artery. The representative examples were shown in Figure 4.1 to Figure 4.3.

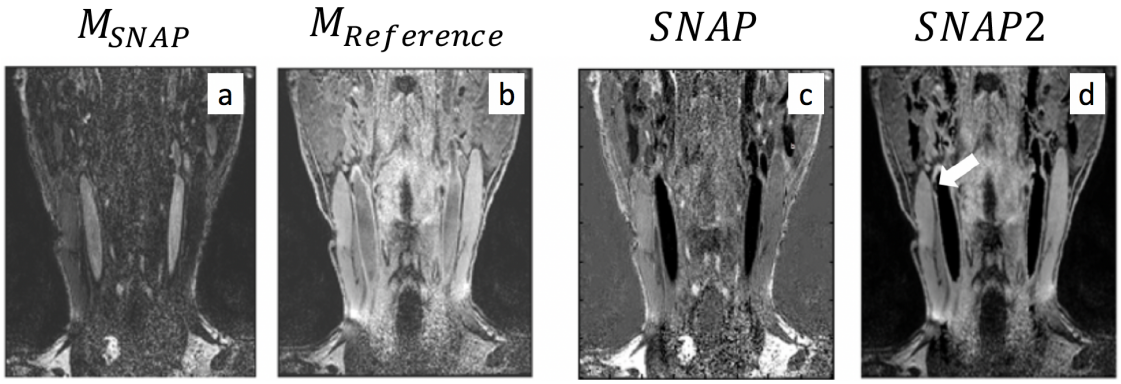

Figure 4.1: (a) and (b) are the magnitude of SNAP MRA and its reference image respectively. (c) is the SNAP MRA and (d) is the black-blood PD weighted image(SNAP2). A juxstaluminal calcification is found in the SNAP2 image (white arrow).

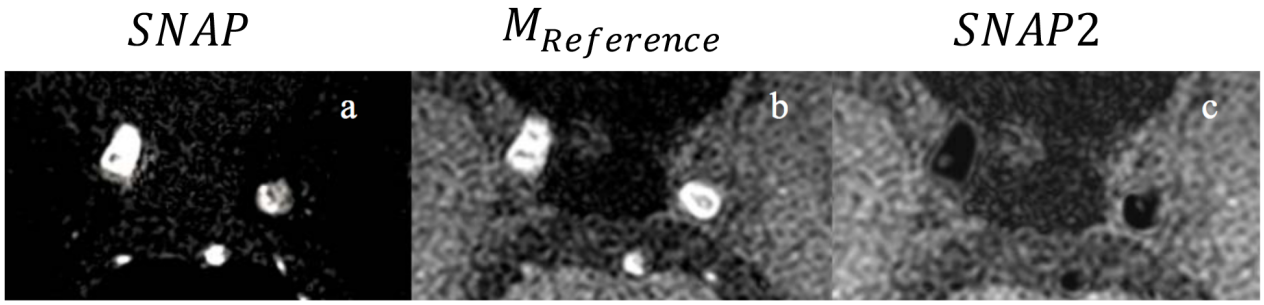

Figure 4.2: SNAP of intracranial artery from a healthy volunteer. (a) is the SNAP MRA, (b) is the M2 of the slice; and (c) is the SNAP2 images.

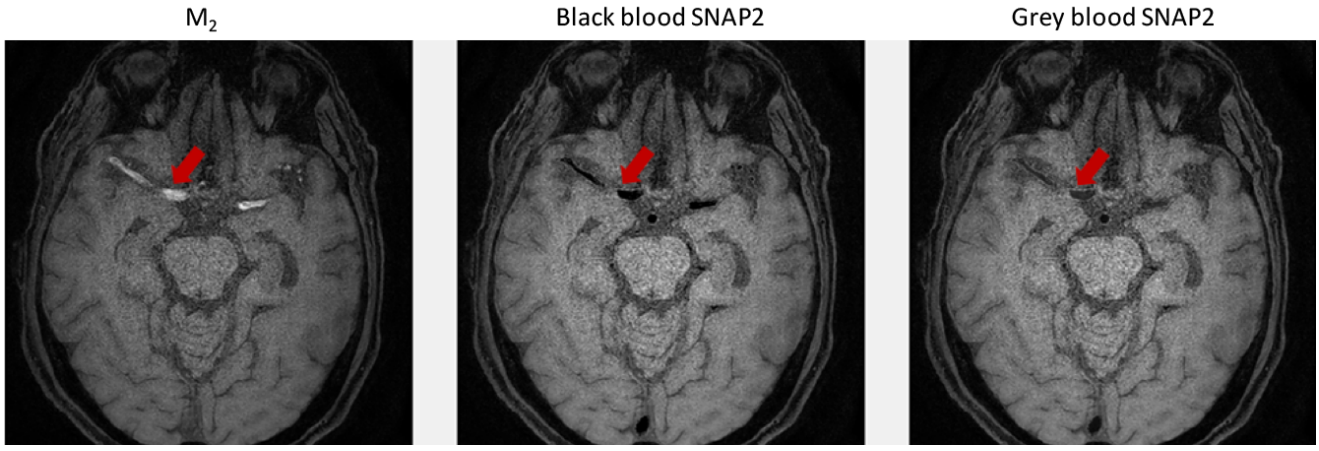

Figure 4.3: With the black blood SNAP2 and M_2, the grey blood SNAP2 can be calculated through the average of them

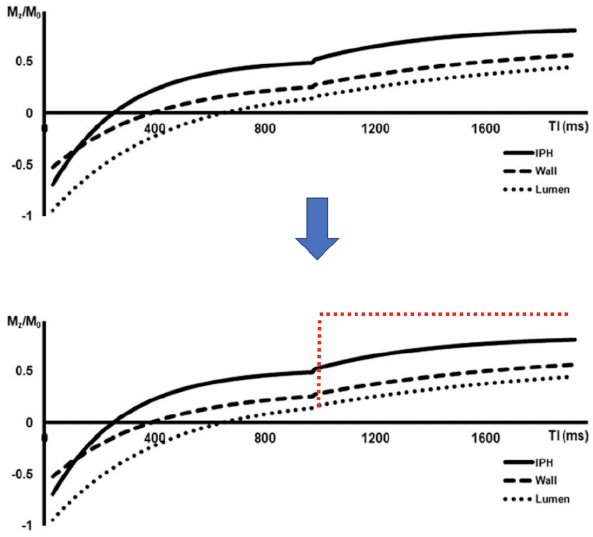

Figure 4.4: (a) The theoretical release trajectory of lumen, vessel wall and IPH during SNAP acquisition. In reality, due to the faster flow rate, at TI of reference scan, the lumen within the FOV is filled with fresh blood(red dotted line) and shows hyperintense signal in the reference image (b)

4.2.2 Grey-blood PD weighted image with intracranial arteries

Flow speed is faster in the intracranial artery than in the carotid artery. The average flow velocity is around 60cm/s[78]in MCA and is only 37.5cm/s in the internal carotid artery [79]. Because of the faster flow speed in the intracranial artery, at TI of reference scan, lumen within the FOV is filled with fresh blood and thereby has hyper-intense signal in the reference image (Figure 4.4). This may cause the partial volume artifacts around the bone structure (Figure 4.5, red arrow).

Figure 4.5: Example of the partial volume artifacts caused by the hyperintense lumen in the reference image of intracranial SNAP. The dark region (red arrow) is part of a bone structure instead of calcification.

To settle this problem, SNAP-MSDE was developed to suppress the lumen signal in the reference image of intracranial artery.

SNAP-MSDE sequence

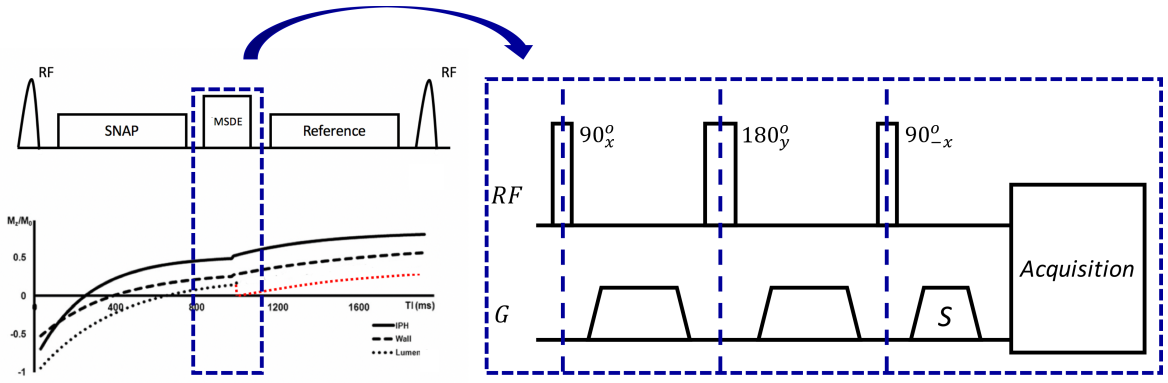

Figure 4.6: SNAP-MSDE sequence: MSDE preparation pulse(right) was inserted before the reference scan of SNAP to suppress the fresh blood in the lumen

Motion sensitized driven equilibrium (MSDE) sequence [80, 81] is a black blood MRA technique(right,Figure 4.6). Flow sensitive gradient pairs are used to suppress the signal with non-zero first order movements while keeping the MRI signal of static tissue unchanged

[80, 81, 82]. MSDE can well suppress the blood signal at the region with turbulent flow [80, 81, 82].

To suppress the fresh blood signal in the reference image, a non-selective MSDE preparation pulse was inserted between the T1 weighted scan and reference scan(Figure 4.6). Right after the iMSDE preparation pulse, the blood is fully suppressed. At TI of reference image, the blood signal is partially recovered to produce the grey blood PD weighted image.

Figure 4.7 shows one intracranial SNAP image from a volunteer scanned with both conventional SNAP and SNAP-MSDE. The black regions(red and yellow arrows) that look like calcification in SNAP reference image are actually part of bone structure in the SNAP-MSDE reference image.

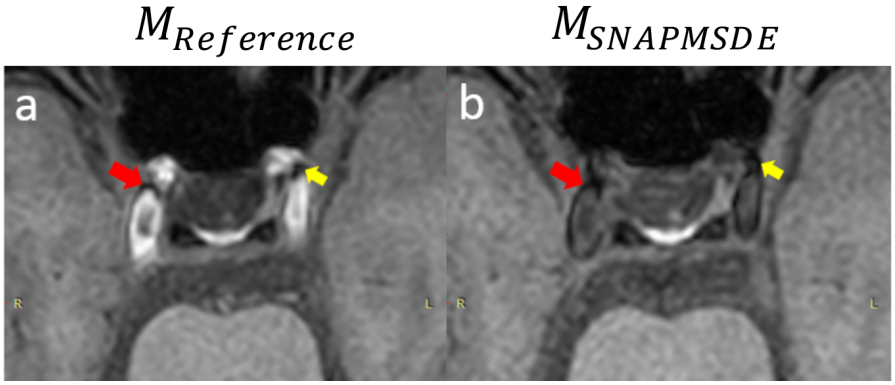

Figure 4.7: Demonstration of the magnitude of the reference images from a volunteer scanned with both regular SNAP(a), bright blood) and SNAP-MSDE(b), grey blood). The black regions(red and yellow arrows) that look like calcifications on SNAP reference image are actually part of bone structure in the SNAP-MSDE reference image

4.3 Improved SNAP with venous flow suppression(iSNAP)

One limitation of SNAP sequence is its inability to differentiate the veins from arteries. Venous contamination will become a challenge for studies that focus only on the pathological characteristics of arteries. To fill this gap, a binary mask-based improved SNAP (iSNAP) method was developed to suppress the venous lumen signal.

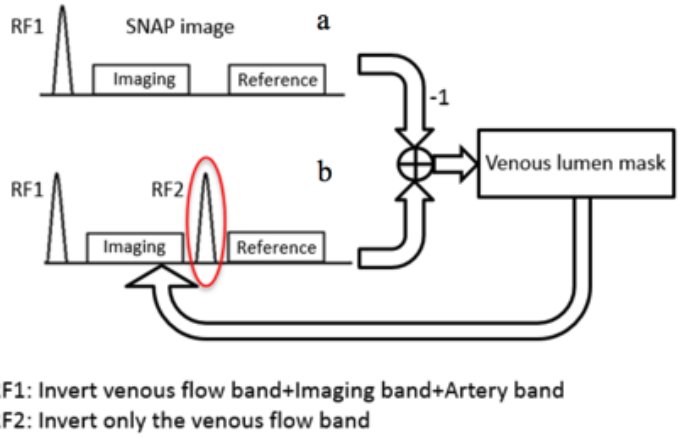

Figure 4.8: SNAP with venous flow suppression. Two images need to be acquired: one regular SNAP MRA (a) and one image scanned with a new SNAP sequence which has an extra inversion pulse (b). The difference between these two SNAP MRA is used as a mask to suppress the venous lumen signal

Sequence design

For iSNAP, two images are collected: One regular SNAP MRA(Figure 4.8 a) and one image scanned with a new SNAP sequence that has an extra inversion pulse (RF2) applied before the reference scan (Figure 4.8b). This extra inversion pulse applied only on the venous suppression region (Figure 4.9b) which changes the release trajectory of vein signal in the steady state without influencing the MRI signal of other tissues. The difference between the two SNAP MRA is used as a mask to suppress the venous signal in the combined SNAP images. These two scans are interleaved to minimize the motion.

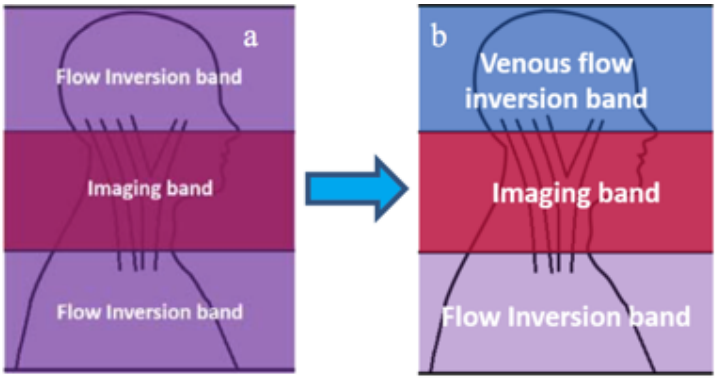

Figure 4.9: The coverage of inversion RF pulse. (a) is the coverage of RF in regular SNAP and (b) is the coverage of RF pulse specific for venous blood suppression

Image post-processing

Between the two SNAP MRA images, only the intensity of venous lumen is different. The difference is transferred to a binary mask to suppress the venous lumen signal in the combined SNAP images. The flow chart of the iSNAP is shown in Figure 4.10.

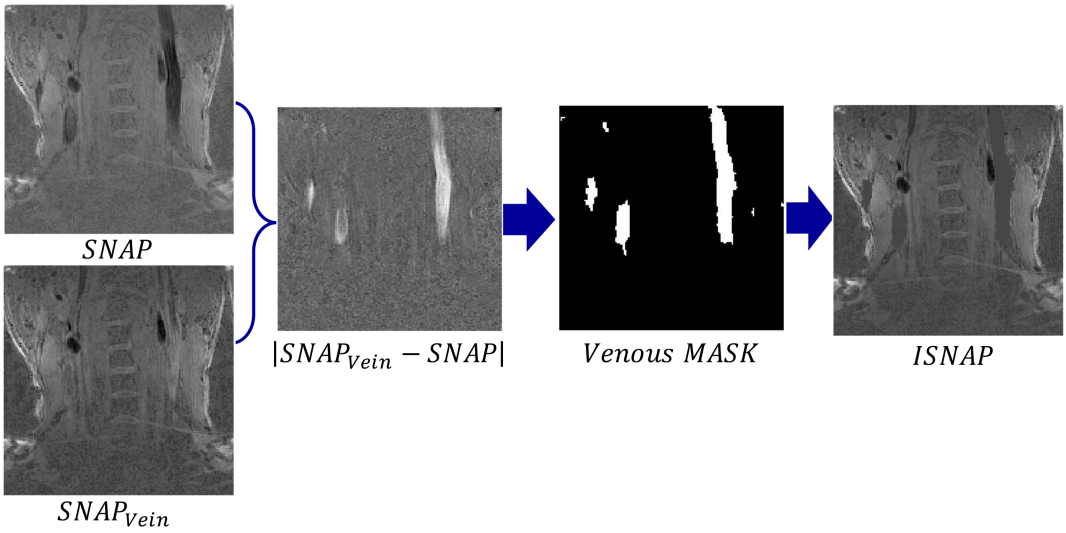

Figure 4.10: The flow chart of iSNAP. Two SNAP images were acquired without and with an extra venous flow suppression RF pulse. The difference is transferred to a binary mask and used to suppress the venous lumen signal in the combined SNAP image

Reconstruction with SAKE

Two scans required by iSNAP will prolong the scan time. To keep the scan time identical with regular SNAP, only half of the k-space was acquired for each SNAP image and SAKE [83] was used for image reconstruction in this study.

MRI scan

Experimental scans were conducted on healthy volunteers with a 3T whole body scanner (Philips Achieva, R3.2.1, the Netherlands). The coil used in this study is a 36-channel neurovascular coil. The scan parameters for iSNAP were: IRTR: 1992ms, TR/TE: 9.9/4.8ms, FA: 11^o, FOV: 160x160x32mm^3, acquired matrix size: 1x1x1mm^3, interpolated to 0.5x0.5x0.5mm^3. 3D images from both SNAP and iSNAP were acquired and transformed to MIP images for comparison. The result is shown in Figure 4.11.

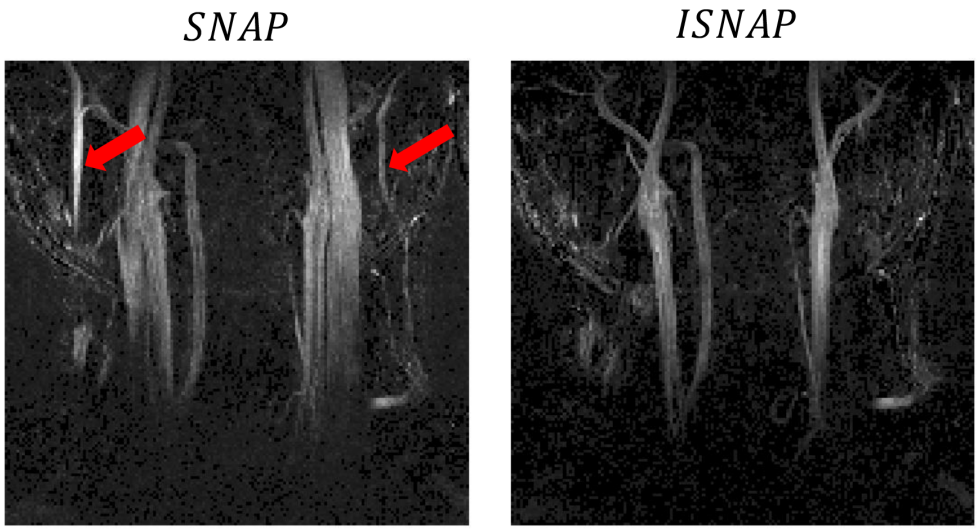

Figure 4.11: Comparison between MIP images of the carotid artery with (right) and without (left) venous suppression pulse. In regular SNAP, both arterial (white arrow) and venous lumens (red arrow) are bright. For iSNAP, the arterial lumen is bright while venous lumen signal is suppressed.

4.4 Summary

In this chapter, SNAP was improved in three aspects. First, the lumen contour identified by the negative polarity of SNAP MRA was transferred in the magnitude of reference image to produce a grey blood PD weighted image(SNAP2) which can be used to detect the calcified nodules near the thin fibrous cap. Secondly, thanks to the fast flow velocity in the intracranial arteries, SNAP2 images in the intracranial arteries were directly produced assisted by the MSDE preparation pulse. And the SNAP MSDE images can help separate the bone structure with calcified nodules. Third, iSNAP was developed to enable SNAP to separate veins from arteries assisted by the artificially constructed binary mask.

Chapter 5

CONCLUSION

5.1 Study Contribution

In this thesis, phase sensitive reconstruction was optimized in three aspects.
First, a three-tier stacks bank was developed to optimize region-growing track for direct phase sensitive reconstruction without reference scan. Compared with existed phase based region-growing methods, such as RAPID, 3D-TRIPS has several advantages:

First, supported by Monte-Carlo simulation, SNR or signal intensity is used to optimize the region growing track and therefore minimizes the error transferred from the low SNR voxels to high SNR voxels. While the phase based region growing methods, such as RAPID, did not take into consideration of the preexisted phase difference and polarity of phase difference. Thus, high SNR voxels are still sensitive to the error transferred from low SNR voxels with RAPID reconstruction.

Second, several randomization measures are used to promote even distribution of region growing track. With these randomization measures, the spatial correlation between successive voxels is minimized. If an error happens on a low SNR voxel, its influence will be offset by the neighboring good voxels.

Third, RAPID needs to sort the voxels according to their phase difference.RAPID is therefore slow and not eligible for 3D large FOV imaging. 3D-TRIPS does not need to sort the voxels and can process 3D image faster. In addition, the better connection of high SNR structures in 3D images can further reduce the error propagation from high SNR to low SNR voxels.

In addition to myocardial LGE imaging, 3D TRIPS can be used for other applications including SNAP and Dixon water-fat separation and quantification.

In the second part of this thesis, SNAP MRA was used as an example to evaluate the accuracy of tissue contour identified by the polarity map of phase sensitive image. This study shows that lumen identified by the negative polarity map of SNAP has a good agreement with CE-MRA thanks to its insensitivity to turbulent flow. Therefore, SNAP MRA can potentially serve as an alternative to TOF and serves as the basis for the development of new automatic lumen segmentation methods. More importantly, this study proves that with optimized acquisitions, tissues of interest can be reliably identified by polarity of phase sensitive images.

In the last part of this thesis, SNAP was improved in three aspects. First, since polarity map of SNAP MRA is proved to be reliable on lumen contour identification, grey blood PD weighed images(SNAP2) were produced by transferring the lumen contour from SNAP MRA to PD weighted reference image. Second, SNAP2 were directly produced with SNAP-MSDE sequence. Calcified nodules near fibrous cap can be detected with SNAP2 images and therefore improve the efficiency and capability of SNAP. Third, iSNAP was developed to enable SNAP for venous lumen suppression assisted by the artificially constructed polarity mask.

5.2 Future work

3D-TRIPS provides a new strategy to estimate the background phase in a fast and robust fashion. The next step will be the development of clinically accessible tool that can be implemented in the scanner system. Another potential work related to 3D-TRIPS is its application on SNAP or Dixon water-fat quantification. SNAP, is even more suitable for 3D-TRIPS than myocardial LGE imaging: First, the TI of SNAP is fixed and the sequence is optimized that lumen is negative with large signal intensity, IPH is positive with large intensity and the other tissues have relative small intensity. The TI of myocardial LGE, on the other hand, is selected case by case and so is the polarity distribution in myocardium. In addition to phase images of inversion recovery images, he background phase of SNAP images can be calculated faster and more robustly by including the intensity information.

In the second part of this thesis, the negative polarity map is proved to be reliable to identify the lumen contour. New automatic lumen detection and segmentation methods as well as the automatic stenosis measurement methods can be developed based on SNAP MRA. SNAP can be further optimized to improve the SNR of vessel wall and thereby reduce the impact of low SNR voxels on the lumen contour identification. Besides, the polarity map can be used to accelerate the SNAP acquisition. The binary polarity map is sparser than respective continuous images and is therefore more suitable for compressed sensing acceleration.

In the third part of this thesis, further validation and optimization of the three methods are still needed. Both iSNAP and SNAP-MSDE can be combined together or with other sequence to identify more risk factors using one single scan.

BIBLIOGRAPHY

[1] E Mark Haacke, Yingbiao Xu, Yu-Chung N Cheng, and Jürgen R Reichenbach. Susceptibility weighted imaging (swi). *Magnetic resonance in medicine*, 52(3):612–618, 2004.

[2] E Mark Haacke, S Mittal, Z Wu, Jaladhar Neelavalli, and Y-CN Cheng. Susceptibility-weighted imaging: technical aspects and clinical applications, part 1. *American Journal of Neuroradiology*, 30(1):19–30, 2009.

[3] Scott B Reeder, Angel R Pineda, Zhifei Wen, Ann Shimakawa, Huanzhou Yu, Jean H Brittain, Garry E Gold, Christopher H Beaulieu, and Norbert J Pelc. Iterative decomposition of water and fat with echo asymmetry and least-squares estimation (ideal): application with fast spin-echo imaging. *Magnetic resonance in medicine*, 54(3):636–644, 2005.

[4] Jinnan Wang, Huijun Chen, Jeffrey H Maki, Xihai Zhao, Gregory J Wilson, Chun Yuan, and Peter Börnert. Referenceless acquisition of phase-sensitive inversion-recovery with decisive reconstruction (rapid) imaging. *Magnetic resonance in medicine*, 72(3):806–815, 2014.

[5] Klaas P Pruessmann, Markus Weiger, Markus B Scheidegger, Peter Boesiger, et al. Sense: sensitivity encoding for fast mri. *Magnetic resonance in medicine*, 42(5):952–962, 1999.

[6] Peter Kellman, Andrew E Arai, Elliot R McVeigh, and Anthony H Aletras. Phase-sensitive inversion recovery for detecting myocardial infarction using gadolinium-delayed hyperenhancement. *Magnetic Resonance in Medicine*, 47(2):372–383, 2002.

[7] Scott B Reeder, Zhifei Wen, Huanzhou Yu, Angel R Pineda, Garry E Gold, Michael Markl, and Norbert J Pelc. Multicoil dixon chemical species separation with an iterative least-squares estimation method. *Magnetic Resonance in Medicine*, 51(1):35–45, 2004.

[8] Jinnan Wang, Peter Börnert, Huilin Zhao, Daniel S Hippe, Xihai Zhao, Niranjan Balu, Marina S Ferguson, Thomas S Hatsukami, Jianrong Xu, Chun Yuan, et al. Simultaneous noncontrast angiography and intraplaque hemorrhage (snap) imaging for carotid atherosclerotic disease evaluation. *Magnetic resonance in medicine*, 69(2):337–345, 2013.

[9] Shanthi Mendis, Pekka Puska, Bo Norrving, et al. *Global atlas on cardiovascular disease prevention and control.* World Health Organization, 2011.

[10] Atherosclerosis. *https://en.wikipedia.org/wiki/Atherosclerosis.*

[11] D Dollemore. Aging hearts and arteries: a scientific quest. *National Institute on Aging. Recuperado de: http://www. niapublications. org/pubs/hearts/Aging_Hearts_And_Arteries. pdf*, 2005.

[12] What is atherosclerosis? *https://www.nhlbi.nih.gov/health/health-topics/topics/atherosclerosis.*

[13] Morteza Naghavi, Peter Libby, Erling Falk, S Ward Casscells, Silvio Litovsky, John Rumberger, Juan Jose Badimon, Christodoulos Stefanadis, Pedro Moreno, Gerard Pasterkamp, et al. From vulnerable plaque to vulnerable patient. *Circulation*, 108(14):1664–1672, 2003.

[14] Dariush Mozaffarian, Emelia J Benjamin, Alan S Go, Donna K Arnett, Michael J Blaha, Mary Cushman, Sandeep R Das, Sarah de Ferranti, Jean-pierre Després, Heather J Fullerton, et al. Executive summary: Heart disease and stroke statistics-2016 update: A report from the american heart association. *Circulation*, 133(4):447, 2016.

[15] Myocardial infarction. *https://en.wikipedia.org/wiki/Myocardial_infarction.*

[16] Arie Franco, Saeed Javidi, and Stefan G Ruehm. Delayed myocardial enhancement in cardiac magnetic resonance imaging. *Journal of radiology case reports*, 9(6):6, 2015.

[17] Aya Kino, Sven Zuehlsdorff, John J Sheehan, Peter J Weale, Timothy J Carroll, Renate Jerecic, and James C Carr. Three-dimensional phase-sensitive inversion-recovery turbo flash sequence for the evaluation of left ventricular myocardial scar. *American Journal of Roentgenology*, 193(5):W381–W388, 2009.

[18] Daniel Peukert, Michael Laule, Matthias Taupitz, Nicola Kaufels, Bernd Hamm, and Marc Dewey. 3d and 2d delayed-enhancement magnetic resonance imaging for detection of myocardial infarction: preclinical and clinical results. *Academic radiology*, 14(7):788–794, 2007.

[19] Rafael Lozano, Mohsen Naghavi, Kyle Foreman, Stephen Lim, Kenji Shibuya, Victor Aboyans, Jerry Abraham, Timothy Adair, Rakesh Aggarwal, Stephanie Y Ahn, et al. Global and regional mortality from 235 causes of death for 20 age groups in 1990 and 2010: a systematic analysis for the global burden of disease study 2010. *The Lancet*, 380(9859):2095–2128, 2013.

[20] Sudha Seshadri and Philip A Wolf. Lifetime risk of stroke and dementia: current concepts, and estimates from the framingham study. *The Lancet Neurology*, 6(12):1106–1114, 2007.

[21] CLM Sudlow, CP Warlow, et al. Comparable studies of the incidence of stroke and its pathological types. *Stroke*, 28(3):491–499, 1997.

[22] Debbie Summers, Anne Leonard, Deidre Wentworth, Jeffrey L Saver, Jo Simpson, Judith A Spilker, Nanette Hock, Elaine Miller, Pamela H Mitchell, et al. Comprehensive overview of nursing and interdisciplinary care of the acute ischemic stroke patient. *Stroke*, 40(8):2911–2944, 2009.

[23] Association AH. ischemic stroke.

[24] Association AH. ischemic strokes(clots). *http* : *//www.strokeassociation.org/STROKEORG/AboutStroke /TypesofStroke/IschemicClots/IschemicStrokesClots_UCM*$_3$*10939_Article.jsp.*

[25] Seemant Chaturvedi and Ralph L Sacco. How recent data have impacted the treatment of internal carotid artery stenosis. *Journal of the American College of Cardiology*, 65(11):1134–1143, 2015.

[26] Tobias Saam, Thomas S Hatsukami, Norihide Takaya, Baocheng Chu, Hunter Underhill, William S Kerwin, Jianming Cai, Marina S Ferguson, and Chun Yuan. The vulnerable, or high-risk, atherosclerotic plaque: Noninvasive mr imaging for characterization and assessment 1. *Radiology*, 244(1):64–77, 2007.

[27] Hunter R Underhill, Thomas S Hatsukami, Zahi A Fayad, Valentin Fuster, and Chun Yuan. Mri of carotid atherosclerosis: clinical implications and future directions. *Nature Reviews Cardiology*, 7(3):165–173, 2010.

[28] Andrew C Newby and Alla B Zaltsman. Fibrous cap formation or destruction?the critical importance of vascular smooth muscle cell proliferation, migration and matrix formation. *Cardiovascular research*, 41(2):345–360, 1999.

[29] Majid M Mughal, Mohsin K Khan, J Kevin DeMarco, Arshad Majid, Fadi Shamoun, and George S Abela. Symptomatic and asymptomatic carotid artery plaque. *Expert review of cardiovascular therapy*, 9(10):1315–1330, 2011.

[30] Norihide Takaya, Chun Yuan, Baocheng Chu, Tobias Saam, Nayak L Polissar, Gail P Jarvik, Carol Isaac, Judith McDonough, Cynthia Natiello, Randy Small, et al. Presence of intraplaque hemorrhage stimulates progression of carotid atherosclerotic plaques. *Circulation*, 111(21):2768–2775, 2005.

[31] Jean-Baptiste Michel, José Luis Martin-Ventura, Antonino Nicoletti, and Benoit Ho-Tin-Noé. Pathology of human plaque vulnerability: mechanisms and consequences of intraplaque haemorrhages. *Atherosclerosis*, 234(2):311–319, 2014.

[32] HR Underhill, Chun Yuan, VL Yarnykh, Baocheng Chu, M Oikawa, Li Dong, NL Polissar, Gwenn A Garden, SC Cramer, and TS Hatsukami. Predictors of surface disruption with mr imaging in asymptomatic carotid artery stenosis. *American Journal of Neuroradiology*, 31(3):487–493, 2010.

[33] Mark M Kockx, Kristel M Cromheeke, Michiel WM Knaapen, Johan M Bosmans, Guido RY De Meyer, Arnold G Herman, and Hidde Bult. Phagocytosis and macrophage activation associated with hemorrhagic microvessels in human atherosclerosis. *Arteriosclerosis, thrombosis, and vascular biology*, 23(3):440–446, 2003.

[34] Jin Hee Yu, Hyo Sung Kwak, Gyung Ho Chung, Seung Bae Hwang, Mi Sung Park, and Seong Hoon Park. Association of intraplaque hemorrhage and acute infarction in patients with basilar artery plaque. *Stroke*, 46(10):2768–2772, 2015.

[35] Gerard Pasterkamp and Mat Daemen. Circulating cells: the biofactory for markers of atherosclerotic disease, 2008.

[36] Roberto Wayhs, Allan Zelinger, and Paolo Raggi. High coronary artery calcium scores pose an extremely elevated risk for hard events. *Journal of the American College of Cardiology*, 39(2):225–230, 2002.

[37] Kelvin KL Wong, Pongpat Thavornpattanapong, Sherman CP Cheung, Zhonghua Sun, and Jiyuan Tu. Effect of calcification on the mechanical stability of plaque based on a three-dimensional carotid bifurcation model. *BMC cardiovascular disorders*, 12(1):7, 2012.

[38] Ajay Gupta, Alvin I Mushlin, Hooman Kamel, Babak B Navi, and Ankur Pandya. Cost-effectiveness of carotid plaque mr imaging as a stroke risk stratification tool in asymptomatic carotid artery stenosis. *Radiology*, 277(3):763–772, 2015.

[39] A Gupta, H Baradaran, and AD Schweitzer. Carotid plaque mri and stroke risk: A systematic review and meta-analysis. *Journal of Vascular Surgery*, 59(4):1175, 2014.

[40] Andrew N Nicolaides, Stavros K Kakkos, Efthyvoulos Kyriacou, Maura Griffin, Michael Sabetai, Dafydd J Thomas, Thomas Tegos, George Geroulakos, Nicos Labropoulos, Caroline J Doré, et al. Asymptomatic internal carotid artery stenosis and cerebrovascular risk stratification. *Journal of vascular surgery*, 52(6):1486–1496, 2010.

[41] Henry JM Barnett, D Wayne Taylor, Michael Eliasziw, Allan J Fox, Gary G Ferguson, R Brian Haynes, Richard N Rankin, G Patrick Clagett, Vladimir C Hachinski, David L Sackett, et al. Benefit of carotid endarterectomy in patients with symptomatic moderate or severe stenosis. *New England Journal of Medicine*, 339(20):1415–1425, 1998.

[42] Michael D Walker, John R Marler, Murray Goldstein, Patricia A Grady, James F Toole, William H Baker, John E Castaldo, Lloyd E Chambless, Wesley S Moore, James T Robertson, et al. Endarterectomy for asymptomatic carotid artery stenosis. *Jama*, 273(18):1421–1428, 1995.

[43] HR Underhill, TS Hatsukami, J Cai, W Yu, JK DeMarco, NL Polissar, H Ota, X Zhao, Li Dong, M Oikawa, et al. A noninvasive imaging approach to assess plaque severity: the carotid atherosclerosis score. *American Journal of Neuroradiology*, 31(6):1068–1075, 2010.

[44] Huilin Zhao, Jinnan Wang, Xiaosheng Liu, Xihai Zhao, Daniel S Hippe, Ye Cao, Jieqing Wan, Chun Yuan, and Jianrong Xu. Assessment of carotid artery atherosclerotic disease by using three-dimensional fast black-blood mr imaging: comparison with dsa. *Radiology*, 274(2):508–516, 2014.

[45] Lippincott Williams et al. North american symptomatic carotid endarterectomy trial. methods, patient characteristics, and progress. *Stroke*, 22(6):711–720, 1991.

[46] Norihide Takaya, Jianming Cai, MT Ferguson, S Marina, Vasily L Yarnykh, Baocheng Chu, Tobias Saam, Nayak L Polissar, Jane Sherwood, Ricardo C Cury, et al. Intra-and interreader reproducibility of magnetic resonance imaging for quantifying the lipid-rich necrotic core is improved with gadolinium contrast enhancement. *Journal of Magnetic Resonance Imaging*, 24(1):203–210, 2006.

[47] Richard Bitar, Alan R Moody, General Leung, Sean Symons, Susan Crisp, Jagdish Butany, Corwyn Rowsell, Alexander Kiss, Andrew Nelson, and Robert Maggisano. In vivo 3d high-spatial-resolution mr imaging of intraplaque hemorrhage 1. *Radiology*, 249(1):259–267, 2008.

[48] John P Mugler and James R Brookeman. Three-dimensional magnetization-prepared rapid gradient-echo imaging (3d mp rage). *Magnetic Resonance in Medicine*, 15(1):152–157, 1990.

[49] Baocheng Chu, Annette Kampschulte, Marina S Ferguson, William S Kerwin, Vasily L Yarnykh, Kevin D O?Brien, Nayak L Polissar, Thomas S Hatsukami, and Chun Yuan. Hemorrhage in the atherosclerotic carotid plaque: a high-resolution mri study. *Stroke*, 35(5):1079–1084, 2004.

[50] Ralph Noeske, Frank Seifert, Karl-Heinz Rhein, and Herbert Rinneberg. Human cardiac imaging at 3 t using phased array coils. *Magnetic resonance in medicine*, 44(6):978–982, 2000.

[51] Raymond J Kim, Edwin Wu, Allen Rafael, Enn-Ling Chen, Michele A Parker, Orlando Simonetti, Francis J Klocke, Robert O Bonow, and Robert M Judd. The use of contrast-enhanced magnetic resonance imaging to identify reversible myocardial dysfunction. *New England Journal of Medicine*, 343(20):1445–1453, 2000.

[52] Chiara Bucciarelli-Ducci, Edwin Wu, Daniel C Lee, Thomas A Holly, Francis J Klocke, and Robert O Bonow. Contrast-enhanced cardiac magnetic resonance in the evaluation of myocardial infarction and myocardial viability in patients with ischemic heart disease. *Current problems in cardiology*, 31(2):128–168, 2006.

[53] Steven G Lloyd and Himanshu Gupta. Assessment of myocardial viability by cardiovascular magnetic resonance. *Echocardiography*, 22(2):179–193, 2005.

[54] Qing-San Xiang. Inversion recovery image reconstruction with multiseed region-growing spin reversal. *Journal of Magnetic Resonance Imaging*, 6(5):775–782, 1996.

[55] Joseph A Borrello, Thomas L Chenevert, and Alex M Aisen. Regional phase correction of inversion-recovery mr images. *Magnetic resonance in medicine*, 14(1):56–67, 1990.

[56] Jingfei Ma. Breath-hold water and fat imaging using a dual-echo two-point dixon technique with an efficient and robust phase-correction algorithm. *Magnetic resonance in medicine*, 52(2):415–419, 2004.

[57] Jingfei Ma, Jong Bum Son, and John D Hazle. An improved region growing algorithm for phase correction in mri. *Magnetic resonance in medicine*, 2015.

[58] Anthony Christopher Davison and David Victor Hinkley. *Bootstrap methods and their application*, volume 1. Cambridge university press, 1997.

[59] Ricardo Otazo, Daniel Kim, Leon Axel, and Daniel K Sodickson. Combination of compressed sensing and parallel imaging for highly accelerated first-pass cardiac perfusion mri. *Magnetic Resonance in Medicine*, 64(3):767–776, 2010.

[60] Daniel K Sodickson, Christopher J Hardy, Yudong Zhu, Randy O Giaquinto, Patrick Gross, Gontran Kenwood, Thoralf Niendorf, Hubert Lejay, Charles A McKenzie, Michael A Ohliger, et al. Rapid volumetric mri using parallel imaging with order-of-magnitude accelerations and a 32-element rf coil array: Feasibility and implications1. *Academic radiology*, 12(5):626–635, 2005.

[61] Samir D Sharma, Caroline L Fong, Brian S Tzung, Meng Law, and Krishna S Nayak. Clinical image quality assessment of accelerated magnetic resonance neuroimaging using compressed sensing. *Investigative radiology*, 48(9):638–645, 2013.

[62] Oren N Jaspan, Roman Fleysher, and Michael L Lipton. Compressed sensing mri: a review of the clinical literature. *The British Journal of Radiology*, 88(1056):20150487, 2015.

[63] David Lesage, Elsa D Angelini, Isabelle Bloch, and Gareth Funka-Lea. A review of 3d vessel lumen segmentation techniques: Models, features and extraction schemes. *Medical image analysis*, 13(6):819–845, 2009.

[64] Jose Biller and William H Thies. When to operate in carotid artery disease. *American family physician*, 61(2):400–410, 2000.

[65] HM Silvennoinen, S Ikonen, L Soinne, M Railo, and L Valanne. Ct angiographic analysis of carotid artery stenosis: comparison of manual assessment, semiautomatic vessel analysis, and digital subtraction angiography. *American journal of neuroradiology*, 28(1):97–103, 2007.

[66] Nicoletta Anzalone, Francesco Scomazzoni, Renata Castellano, Laura Strada, Claudio Righi, Letterio S Politi, Miles A Kirchin, Roberto Chiesa, and Giuseppe Scotti. Carotid artery stenosis: Intraindividual correlations of 3d time-of-flight mr angiography, contrast-enhanced mr angiography, conventional dsa, and rotational angiography for detection and grading 1. *Radiology*, 236(1):204–213, 2005.

[67] JM Wardlaw, FM Chappell, JJK Best, K Wartolowska, E Berry, et al. Non-invasive imaging compared with intra-arterial angiography in the diagnosis of symptomatic carotid stenosis: a meta-analysis. *The Lancet*, 367(9521):1503–1512, 2006.

[68] Mitsue Miyazaki and Vivian S Lee. Nonenhanced mr angiography 1. *Radiology*, 248(1):20–43, 2008.

[69] Claude Levy, Jean Pierre Laissy, Vincent Raveau, Pierre Amarenco, Vincent Servois, Marie Germaine Bousser, and Jean Michel Tubiana. Carotid and vertebral artery dissections: three-dimensional time-of-flight mr angiography and mr imaging versus conventional angiography. *Radiology*, 190(1):97–103, 1994.

[70] Robert R Edelman, Bettina Siewert, Mary Adamis, Jochen Gaa, Gerhard Laub, and Piotr Wielopolski. Signal targeting with alternating radiofrequency (star) sequences: application to mr angiography. *Magnetic resonance in medicine*, 31(2):233–238, 1994.

[71] William Kerwin, Dongxiang Xu, Fei Liu, Tobias Saam, Hunter Underhill, Norihide Takaya, Baocheng Chu, Thomas Hatsukami, and Chun Yuan. Magnetic resonance imaging of carotid atherosclerosis: plaque analysis. *Topics in Magnetic Resonance Imaging*, 18(5):371–378, 2007.

[72] Ye Qiao, David A Steinman, Maryam Etesami, Alex Martinez-Marquese, Edward G Lakatta, and Bruce A Wasserman. Impact of t2 decay on carotid artery wall thickness measurements. *Journal of Magnetic Resonance Imaging*, 37(6):1493–1498, 2013.

[73] Robert L Greenman, Xiaoen Wang, Long Ngo, Robert P Marquis, and Norman Farrar. An assessment of the sharpness of carotid artery tissue boundaries with acquisition voxel size and field strength. *Magnetic resonance imaging*, 26(2):246–253, 2008.

[74] Harald Kramer, Val M Runge, John N Morelli, Kenneth D Williams, L Gill Naul, Konstantin Nikolaou, Maximilian F Reiser, and Bernd J Wintersperger. Magnetic resonance angiography of the carotid arteries: comparison of unenhanced and contrast enhanced techniques. *European radiology*, 21(8):1667–1676, 2011.

[75] Charles M Anderson, David Saloner, Jay S Tsuruda, Lorraine G Shapeero, and Ralph E Lee. Artifacts in maximum-intensity-projection display of mr angiograms. *AJR. American journal of roentgenology*, 154(3):623–629, 1990.

[76] Cornelis M van Bemmel, Otto EH Elgersma, Evert-jan PA Vonken, Marco Fiorelli, Maarten S van Leeuwen, and Wiro J Niessen. Evaluation of semiautomated internal carotid artery stenosis quantification from 3-dimensional contrast-enhanced magnetic resonance angiograms. *Investigative radiology*, 39(7):418–426, 2004.

[77] Cornelis M van Bemmel, Max A Viergever, and Wiro J Niessen. Semiautomatic segmentation and stenosis quantification of 3d contrast-enhanced mr angiograms of the internal carotid artery. *Magnetic resonance in medicine*, 51(4):753–760, 2004.

[78] M Farhoudi, SN Kermani, and H Sadeghi-Bazargani. Relatively higher norms of blood flow velocity of major intracranial arteries in north-west iran. *BMC research notes*, 3(1):174, 2010.

[79] L Aldo Ferrara, Marcello Mancini, Rita Iannuzzi, Teodoro Marotta, Iole Gaeta, Fabrizio Pasanisi, Alfredo Postiglione, and Lucio Guida. Carotid diameter and blood flow velocities in cerebral circulation in hypertensive patients. *Stroke*, 26(3):418–421, 1995.

[80] Jinnan Wang, Vasily L Yarnykh, and Chun Yuan. Enhanced image quality in black-blood mri using the improved motion-sensitized driven-equilibrium (imsde) sequence. *Journal of Magnetic Resonance Imaging*, 31(5):1256–1263, 2010.

[81] Jinnan Wang, Suzanne C Gerretsen, Jeffrey H Maki, Caroline Jaarsma, M Eline Kooi, Daniel Herzka, Baocheng Chu, Vasily L Yarnykh, Chun Yuan, and Tim Leiner. Time-efficient black blood rca wall imaging at 3t using improved motion sensitized driven equilibrium (imsde): feasibility and reproducibility. *PloS one*, 6(10):e26567, 2011.

[82] Jinnan Wang, Vasily L Yarnykh, Thomas Hatsukami, Baocheng Chu, Niranjan Balu, and Chun Yuan. Improved suppression of plaque-mimicking artifacts in black-blood carotid atherosclerosis imaging using a multislice motion-sensitized driven-equilibrium (msde) turbo spin-echo (tse) sequence. *Magnetic resonance in medicine*, 58(5):973–981, 2007.

[83] Peter J Shin, Peder EZ Larson, Michael A Ohliger, Michael Elad, John M Pauly, Daniel B Vigneron, and Michael Lustig. Calibrationless parallel imaging reconstruction based on structured low-rank matrix completion. *Magnetic resonance in medicine*, 72(4):959–970, 2014.

[84] T Scarabino, A Carriero, GM Giannatempo, R Marano, P De Matthaeis, L Bonomo, and U Salvolini. Contrast-enhanced mr angiography (ce mra) in the study of the carotid stenosis: comparison with digital subtraction angiography (dsa). *Journal of neuroradiology. Journal de neuroradiologie*, 26(2):87–91, 1999.

[85] Niranjan Balu, Vasily L Yarnykh, Baocheng Chu, Jinnan Wang, Thomas Hatsukami, and Chun Yuan. Carotid plaque assessment using fast 3d isotropic resolution black-blood mri. *Magnetic resonance in medicine*, 65(3):627–637, 2011.

[86] JM Wardlaw, FM Chappell, M Stevenson, E De Nigris, S Thomas, J Gillard, E Berry, G Young, P Rothwell, G Roditi, et al. Accurate, practical and cost-effective assessment of carotid stenosis in the uk. 2006.

[87] Zhaoyang Fan, Wei Yu, Yibin Xie, Li Dong, Lixin Yang, Zhanhong Wang, Antonio Hernandez Conte, Xiaoming Bi, Jing An, Tianjing Zhang, et al. Multi-contrast atherosclerosis characterization (match) of carotid plaque with a single 5-min scan: technical development and clinical feasibility. *Journal of Cardiovascular Magnetic Resonance*, 16(1):53, 2014.

[88] T Saam, MS Ferguson, VL Yarnykh, N Takaya, D Xu, NL Polissar, TS Hatsukami, and Chun Yuan. Quantitative evaluation of carotid plaque composition by in vivo mri. *Arteriosclerosis, thrombosis, and vascular biology*, 25(1):234–239, 2005.

VITA

Haining Liu was born and raised in Laizhou, which is a small city on the eastern coast of China. He obtained both his Master of Science and Bachelor of Engineering degrees from the Electronical Engineering department of Tsinghua University, Beijing, China. He then moved to Seattle and continued his graduate study in the Department of Bioengineering, University of Washington. His currently research focus is the optimization of phase sensitive MRI of cardiovascular diseases.